THE UNIVERSITY of ADELAIDE

School of Physical Sciences

New Physics searches at the High Luminosity LHC

Kaustubh Naik

Supervisors:

Dr. Paul Jackson
Dr Waseem Kamleh

A thesis submitted towards the degree of
Masters of Philosophy
at
The Faculty of Sciences
The University of Adelaide

October, 2015

Abstract

This thesis studies the $\tilde{\chi}_1^{\pm}\tilde{\chi}_1^{\mp}$ and $\tilde{\ell}^{\pm}\tilde{\ell}^{\mp}$ production processes in an upgraded LHC environment at $\sqrt{\hat{s}} = 14$ TeV. The Super Razor variables will be employed to obtain kinematic information and separate these Supersymmetric production processes from Standard Model background with identical final state topology. The analysis will be done using Monte Carlo generated data of events where truth-level information will be smeared to simulate the Phase-I and Phase-II ATLAS detector.

I certify that this work contains no material which has been accepted for the award of any other degree or diploma in my name, in any university or other tertiary institution and, to the best of my knowledge and belief, contains no material previously published or written by another person, except where due reference has been made in the text. In addition, I certify that no part of this work will, in the future, be used in a submission in my name, for any other degree or diploma in any university or other tertiary institution without the prior approval of the University of Adelaide and where applicable, any partner institution responsible for the joint-award of this degree.

I give consent to this copy of my thesis when deposited in the University Library, being made available for loan and photocopying, subject to the provisions of the Copyright Act 1968.

I also give permission for the digital version of my thesis to be made available on the web, via the University's digital research repository, the Library Search and also through web search engines, unless permission has been granted by the University to restrict access for a period of time.

Contents

Chapter 1

Introduction

The study of particle physics could be traced back to the late 1800s, with the discovery of the electron[1]. Over the two centuries we have made many advancements in our knowledge of the composition of the Universe. From atomic models to field theories, our models progressively become more complex and detailed. However our journey is far from over, there are still discoveries to be made, theories to be tested, and many more experiments to run.

Physicists have often used symmetry and algebra to formulate most of our modern theories of particle physics. Often one will hear about the Standard Model (SM)[2–4], a robust model which is widely accepted that explains a lot of our observations. SM consists of elementary particles which can be split into fermions(spin 1/2) and bosons(integer spin). The fermions make up matter and can be subdivided into leptons and quarks. They are also grouped into three generations, with four fermions in each generation. The first generation is the most stable and the third generation the least stable. The bosons are considered to be the force carriers, they mediate the electromagnetic, strong and weak interactions between the elementary particles.

Since the discovery of the Higgs boson[5–7] (or god particle if you are more familiar with sensationalist media) you may naively think that SM is the complete picture of the subatomic Universe. Unfortunately SM provides no candidate for Dark Matter, and has a hierarchy problem in the Higgs field. There is substantial reason to believe that we should extend SM.

Creating a supersymmetric extension of SM is a method of tackling these modern issues. We create supersymmetric partners for each of SM particles, a boson for each fermion and a fermion for each boson. This symmetry between the fermions and bosons is what we call Supersymmetry(SUSY)[8–16]. The simplest model in which we extend SM with SUSY is called Minimal Supersymmetric Standard Model(MSSM).

If we are to discover new physics it will most likely occur at a particle accelerator, like the Large Hadron Collider (LHC). From the collisions of energetic particles we obtain the kinematics of outgoing observable particles through a series of detectors. The analysis of these kinematics usually reveal the underlying physics, through this process we have discovered many of SM particles. Unfortunately we have yet to discover SUSY at any particle collider. A series of upgrades will raise both the energy and intensity of the LHC's proton-proton collisions. Upgrades to the LHC experiments, such as the ATLAS[17] detector, are required to interrogate these groundbreaking conditions.

In this thesis I will describe SM and SUSY in more detail, the allowed possible interactions and how SUSY can resolve issues of SM. The LHC, the ATLAS detector and the upgrade will also be described, with concentration on the components relevant to our particular analysis. I will also describe the kinematic variables that will be used in the analysis, and the advantages these pose in contrast to previous studies for new physics searches at the upgraded LHC. The data used in the analysis will be outlined, the process of generating events and the simulation of the upgraded ATLAS detector. The final results will show the effectiveness of the selected kinematic variables at identifying new physics in a simulation of the upgraded LHC.

Chapter 2

Standard Model and Supersymmetry

2.1 Standard Model

In nature we have observed four fundamental forces. Ordered from largest interaction range to lowest they are:

- Gravity, responsible for the attraction between masses.
- Electromagnetic, responsible for the attraction between opposite charges and like charges repelling.
- Weak, responsible for nuclear decays.
- Strong, responsible for stability of nuclei.

The interaction length of the electromagnetic, weak and strong forces are significantly smaller than that of gravity. SM is a theory that describes the electromagnetic, weak and strong forces but does not describe gravity. Currently SM is the most accepted theory for physics at the quantum scale, however physicists are aware that SM does not completely describe all phenomena at the quantum scale.

SM describes each of the interactions as a quantum field theory. The smallest possible perturbations (quanta) of these fields are what we call particles. These particles have properties which make them distinct, their mass, charge and spin.

For the weak interactions we have the W and Z bosons, for electromagnetic interactions we have the photon, and the gluon for strong interactions. All of these particles are referred to as gauge bosons, and have spin 1.

Matter particles are affected by these interaction fields, and are also described by field theories. These matter particles are referred to as fermions and have spin 1/2. The gauge bosons interact through certain properties of the fermions, for instance the charge of the fermion allows photons to 'couple' to the fermion field. The colour (colour here is used to describe another type of charge, it has no relation to the visible spectrum of light) of the quarks allow for interaction with the gluon.

As a result of the Dirac equation, antimatter was also predicted[18]. Antimatter is made of antiparticles which have the same mass as their matter counter part but have opposite charge and quantum numbers. Antiparticles are given the same name as their matter counter part with prefix 'anti-' and use the same label except with a bar above it. For instance the anti-top is the antiparticle of the top quark and is labelled $\bar{t}$.

The fermions can be divided into three generations, each generation containing two quarks and two leptons. The 1st generation contains the lightest particles and the 3rd generation contain the heaviest particles. In each generation there is a charged lepton and a neutral lepton labelled the neutrino. There is a quark with charge +2/3e and -1/3e (where 'e' is the elementary electric charge) in each generation. We label these six quarks as having different flavour, in order to distinguish each elementary quark. The weak bosons can interact with these fermions and change their flavour.

Due to confinement by the strong force, quarks are not observed by themselves. Quarks are confined into groups of two or three to make either a meson or a baryon respectively. These grouped quarks are called hadrons.

The Higgs field explains why the weak field has a short range in comparison to gravity and electromagnetic interactions. The theory is constructed such that the bosons associated with the weak interaction are given mass, as well as the quarks and leptons. The mediator of the Higgs field is called the Higgs boson and is the only boson in SM with spin 0. Figure 2.1 shows all SM particles and their properties.

2.1.1 Feynman Diagrams

Feynman diagrams[20] represent interactions at the elementary level and allow us to visualize and perform calculations with a much simpler set of tools. We call the point in which multiple lines meet a vertex and the lines are referred to as propagators. The propagator represents a particle travelling through space and time, and a vertex represents an interaction between particles. There are conventions for certain styles of lines representing a certain family of particles. In this thesis, we use wavy lines for Electroweak bosons, springs for gluons, straight lines for fermions and dashed straight line for

Higgs boson. For SUSY particles, the propagators are coloured red, sleptons being dashed lines, and SUSY fermions given a straight and wavy line

Depending on the theory, there are vertices which are allowed which can be interpreted as there are only certain interactions allowed. For instance, in Quantum Electrodynamics, the theory that describes electromagnetic interactions, the only allowed vertex is a photon to two fermions.

These diagrams can be read in any direction, though in this thesis we will usually refer to the interaction occurring from left to right. The time axis here is horizontal and moving to the right is increasing in time, though we can flip this in any direction and that interaction should still be allowed. Particles moving backwards in time represent anti-particles.

The Figure 2.2 shows the production of a Higgs boson through two different processes. It illustrates two gluons which can generate a loop of top or bottom quarks which can in turn generate a Higgs boson. The other diagram describes two fermions interacting through the Weak force to create a Higgs boson, the final state also contains the fermions at the beginning.

2.1.2 The Hierarchy Problem

A significant issue with SM is that there exists a hierarchy problem with the non-zero Higgs field. The electrically neutral part of the Standard Model Higgs field is a complex scalar H with a classical potential

$$V = m_H^2|H|^2 + \lambda|H|^2. \tag{2.1}$$

The Standard Model requires a non-vanishing vacuum expectation value (VEV) for H at the minimum of the potential. This will occur if $\lambda > 0$ and $m_H^2 < 0$, resulting in $\langle H \rangle = \sqrt{-m_H^2/2\lambda}$. Since we know experimentally that $\langle H \rangle$ is approximately 174 GeV, from measurements of the properties of the weak interactions, it must be that m_H^2 is very roughly of order $-(100\text{GeV})^2$.

In a vacuum particle and anti-particle pairs are constantly being created and annihilated. We expect these should interact with the Higgs field and contribute to the value of the Higgs field. Figure 2.3 shows the one-loop contributions to m_H^2. Unfortunately this involves adding all the contributions from the different momenta pairs, and we have a divergent sum. We can save ourselves from an infinite mass of the Higgs boson using a cut-off. If the Higgs field couples to f with a term in the Lagrangian $-\lambda_f H\bar{f}f$, then the Feynman diagram in Figure 2.3 yields a correction

$$\Delta m_H^2 = -\frac{|\lambda_f|^2}{8\pi^2}\Lambda_{\text{UV}}^2 + \ldots, \tag{2.2}$$

where $\Lambda_{\rm UV}$ is an ultraviolet momentum cutoff. It is expected that this model is only sensible up to a certain energy scale, however the only cut-off would be around the gravitational scale. The Planck mass is the closest reasonable cut-off but it is around 10^{18} GeV! This discrepancy is what is known as the hierarchy problem.

Furthermore, there are contributions similar to eq. 2.2 from the virtual effects of any arbitrarily heavy particles that might exist, and these involve the masses of the heavy particles, not just the cutoff. For example, suppose there exists a heavy complex scalar particle S with mass m_S that couples to the Higgs with a Lagrangian term $-\lambda_S|H|^2|S|^2$. Then the Feynman diagram of S in Figure 2.3 gives a correction

$$\Delta m_H^2 = \frac{\lambda_S}{16\pi^2}\left[\Lambda_{\rm UV}^2 - 2m_s^2 \ln\left(\Lambda_{\rm UV}/m_S\right) + \ldots\right]. \tag{2.3}$$

If one rejects the possibility of a physical interpretation of $\Lambda_{\rm UV}$ and uses dimensional regularization on the loop integral instead of a momentum cutoff, then there will be no $\Lambda_{\rm UV}^2$ piece. However, even then the term proportional to m_S^2 cannot be eliminated without the physically unjustifiable tuning of a counter-term specifically for that purpose. So m_H^2 is sensitive to the masses of the heaviest particles that H couples to; if m_S is very large, its effects on the on the Standard Model do not decouple, but instead make it difficult to understand why m_H^2 is so small.

The systematic cancellation of the dangerous contributions to Δm_H^2 can only be brought about by the type of conspiracy that is better known to physicists as a symmetry. There are symmetries which relate to the fermions and gauge bosons having a spin that protect their masses from divergences, but SM doesn't provide a symmetry to protect the Higgs field[21].

2.1.3 Dark Matter

Observation of galaxies has shown us that there exists a significant amount of matter that we have not accounted for in SM. There are galaxies that need much more mass than we have observed to stay in their rotation without breaking up. This matter is not luminous and makes up around 24% of the mass in the universe. Particle candidates for Dark Matter are required to be electrically neutral (or interact weakly with other matter) and massive. Candidates are generally referred to as WIMPs (Weakly Interacting Massive Particles). SM does not have a candidate that matches the properties of Dark Matter, this doesn't invalidate SM, but implies we will need physics beyond SM[22].

2.2 Supersymmetry

SUSY[8–16] is a symmetry that can be used to extend SM and solve both the hierarchy problem and provide a candidate for dark matter. For every fermion we create a boson and for every boson we create a fermion. This symmetry cancels out the diverging contribution to the Higgs field vacuum expectation value by design.

The single-particle states of a supersymmetric theory fall into irreducible representations of the supersymmetry algebra, called supermultiplets. Each supermultiplet contains both fermion and boson states, which are commonly known as superpartners of each other. Each supermultiplet contains an equal number of fermion and boson degrees of freedom.

These new SUSY particles have the same charge, weak isospin and colour charges as their superpartners. Since we have yet to observe any SUSY particles, the symmetry must be broken to allow the SUSY particles to have higher masses.

We give the super partners of SM fermions the same name as their SM partners except with a prefix of 's'. For example, the super partner of top would be called stop, for electron we would have selectron. The super partners of SM bosons have the same name with the affix of '-ino'. The wino is the super partner of the W boson, and the higgsino is the super partner of the Higgs boson. There are in fact multiple higgsinos and winos. In our short hand notation we use tildes above SM particle to identify the SUSY particle, the stop is given the label '$\tilde{t}$'. Of interest to this thesis are the charginos ($\tilde{\chi}_i^{\pm}$), neutralinos ($\tilde{\chi}_i^0$) and slepton($\tilde{\ell}^{\pm}$). The charginos are a linear combination of the charged winos and charged higgsinos which gives two mass eigenstates with charge ± 1. The $\tilde{\chi}_1^{\pm}$ is the lighter mass eignestate and the $\tilde{\chi}_2^{\pm}$ is the heavier. The neutralinos are a combination of the neutral higgsino, neutral wino and bino and give four mass eigenstates, where $\tilde{\chi}_1^0$ is the lightest and $\tilde{\chi}_4^0$ is the heaviest.

2.2.1 R-Parity

R-parity is a symmetry of MSSM that naturally eliminate terms that would break baryon number and lepton number conservation, without assuming that these quantum numbers are fundamental symmetries in nature. It is defined as:

$$P_R = (-1)^{3(B-L)+2s} \tag{2.4}$$

where B is baryon number, L is lepton number and s is spin.

This results in SM particles having even R-parity ($P_R = +1$) and SUSY

squarks, sleptons, gauginos, and Higgsinos have odd R-parity ($P_R = -1$)[1]. If R-parity is exactly conserved, then there will be no mixing between SUSY and SM particles, and every interaction vertex will have an even number of SUSY particles. This leads to the following consequences:

- The lightest SUSY particle (LSP) will become absolutely stable.
- Each SUSY particle must decay into a state that contains an odd number of LSPs.
- SUSY particles can only be produced in even numbers.

If the LSP is electrically neutral, it interacts only weakly with ordinary matter, and so can make an attractive candidate for the non-baryonic dark matter that seems to be required by cosmology[21].

2.3 Production processes

Experimentally the particles of interest will be produced through the collision of protons. Of interest are the production of oppositely charged sleptons and charginos with the labelled $\tilde{\ell}^+\tilde{\ell}^-$ and $\tilde{\chi}_1^+\tilde{\chi}_1^-$ respectively. Relatively light charginos and neutralinos have a possible connection to weakly interacting dark matter in supersymmetry models with conserved R-parity. Light sleptons are motivated by the measured value of the anomalous magnetic moment $g-2$ of the muon [23, 24], providing a thermal annihilation cross section for binolike neutralino dark matter [25], and the possibility that the branching fraction of the newly discovered Higgs boson into two photons is enhanced over the Standard Model prediction [26]. Charginos, neutralinos, and sleptons could also appear in cascade decays of heavier colored superpartners, but this prospect merely emphasizes the importance of being able to produce these lighter superpartners directly[27].

We cannot directly detect these particles, instead detect the products of their decay. The final state of the decays are relatively simple, two oppositely charged leptons, and a set of particles which are undetectable by our experimental apparatus, which are collectively grouped and labelled missing energy. As a result of colliding protons we also expect jets, the remaining quarks and gluons from the intial protons will hadronise giving us jets.

[1] in fact you could define a particle as being supersymmetric if it has an odd R-parity.

2.3.1 Di-leptonic decays

Figure 2.4 shows the "di-slepton" production and its decay into neutralinos and leptons. Due to the construction these final leptons will also be the same flavour.

Figure 2.5 shows "di-chargino" production, which decays into W bosons and neutralinos. The W bosons are then expected to decay into leptons and neutrinos. The final state leptons are opposite charge, but unlike the slepton, can be of mixed flavour. In addition to the neutralinos, the neutrinos also contribute to the missing energy.

2.3.2 SM Background

SM processes which produce a final state of oppositely charged leptons with missing energy are considered background to the SUSY signal processes. Pairs of oppositely charged W^+W^- bosons can decay into pairs of same flavour or opposite flavour leptons with their associated neutrino and anti-neutrino. The Z boson can also decay into a lepton anti-lepton pair[29], these are produced with the same flavour. These bosons can be produced directly or indirectly from proton-proton collisions. The Higgs background is comprised of two main production modes, vector boson fusion and gluon fusion. In SM the Higgs boson can decay to pairs of oppositely charged W bosons($H \rightarrow W^+W^-$) with a branching fraction of 0.215[30]. Figure 2.6 shows how gluon interactions from proton collisions could produce a di-leptonic final state. Top pair production decays into oppositely charged W bosons with a pair of bottom quarks nearly 100% of the time[31]. The bottom quarks from this decay hadronise to produce jets, which are b-tagged and referred to as b-jets.

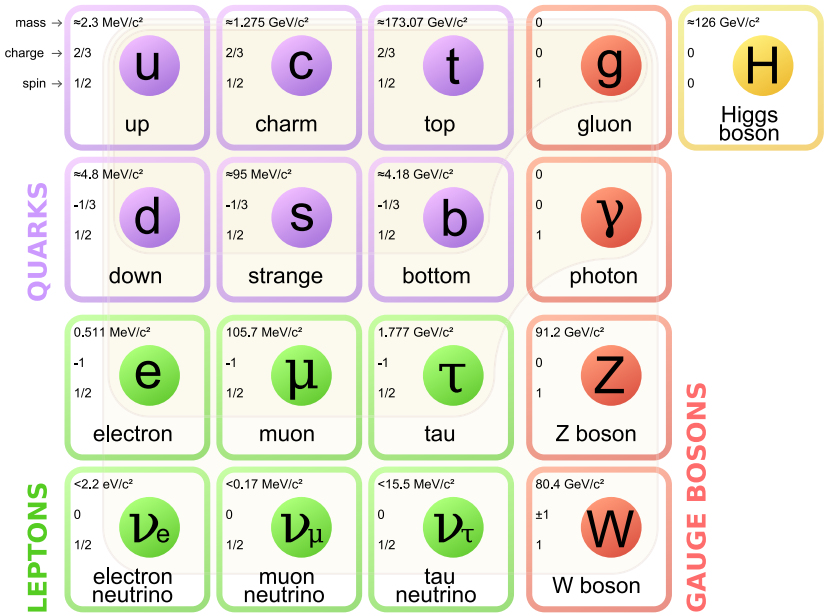

Figure 2.1: SM particles arranged into the classified groups, with the fermions grouped into their generations from left to right. Image courtesy of Fermilab, Office of Science, United States Department of Energy, Particle Data Group.[19]

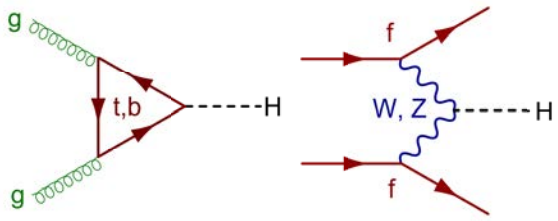

Figure 2.2: Feynman diagrams of gluon fusion on the left and vector boson fusion on the right

Figure 2.3: One-loop quantum corrections to the Higgs squared mass parameter m_H^2, due to a Dirac fermion f(left), and a scalar S(right).

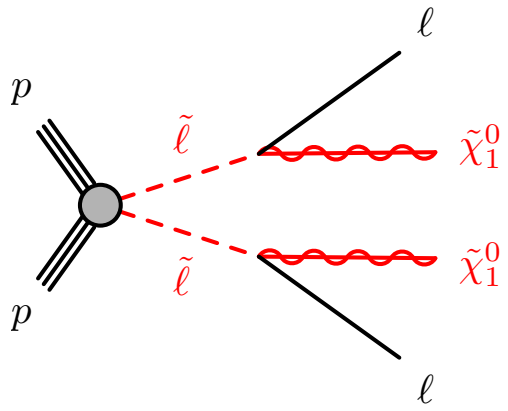

Figure 2.4: Feynman diagram of di-slepton production

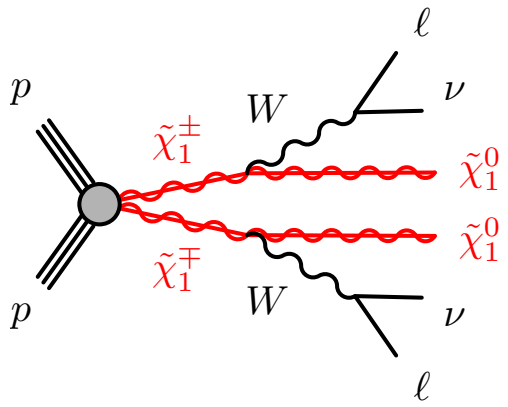

Figure 2.5: Feynman diagram of di-chargino production

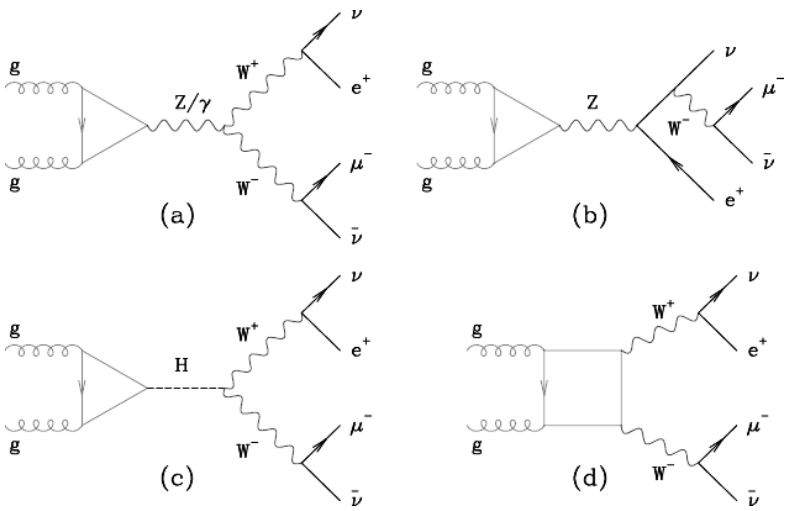

Figure 2.6: Feynman diagrams of W^+W^- production (a,c,d) and a Z boson production with a W boson branch (b) which produce a di-lepton final state (mixed flavour in this case)[28]

Chapter 3

Experimental apparatus

3.1 The Large Hadron Collider

CERN[32], an abbreviation for Conseil Européen pour la Recherche Nucléaire, is a European organization for research in particle physics. CERN is responsible for the largest particle accelerators in the world, aptly called the Large Hadron Collider (LHC).

The LHC is a ring 27 kilometres in circumference. It is situated 100m underground and straddles the Swiss-French border. This machine is made up of two beam pipes in which protons travel around at speeds nearing that of light. There are 1232 dipole magnets, 15 metres in length, which bend the beams, and 392 quadrupole magnets, each 5–7 metres long, which focus the beams[33]. Figure 3.1 shows the cross section of the LHC, with the various components required that allow for protons to travel at enormous speed and energies.

Protons are inserted into the LHC through the accelerator complex, a set of accelerators designed to progressively boost the energy and clump the protons. Two beams of protons enter the two pipes, one beam travelling clockwise, the other anti-clockwise. The pipes intersect and allow collisions at four locations along the LHC. These intersections are fitted with detectors, these are ATLAS[17], CMS[34], ALICE[35] and LHCb[36] seen in Figure 3.2.

3.2 ATLAS

ATLAS[17] is a general purpose detector which is designed to research a diverse range of physics, like Higgs boson searches, dark matter and extra dimensions. The detector weighs up to 7 kilo-tonnes, cylindrical in shape with a height of 25m and length of 44m. A graphic showing the detector and

its various components can be seen in Figure 3.3. The solid angle coverage from the point of collision is almost 4π. The co-ordinate system uses a right hand convention, with the origin at the nominal interaction point in the centre of the detector and the z-axis along the beam pipe. The x-axis points from the interaction point to the centre of the LHC ring, the y-axis points upward. Cylindrical coordinates (r, ϕ) are used in the transverse plane, with r being the radial distance to the z-axis and ϕ being the azimuthal angle around the beam pipe. The pseudo-rapidity is defined in terms of the polar angle θ as $\eta = -\ln[\tan(\theta/2)]$. Closest to the beam-line are inner tracking detectors (ID) which use layers of silicon-based and straw-tube detectors, located inside a superconducting solenoid that provides a 2T magnetic field, to measure the trajectories of charged particles within $|\eta| < 2.5$. The solenoid is surrounded by a hermetic calorimeter system. A liquid argon (LAr) fine-grained sampling electromagnetic (EM) calorimeter with excellent energy resolution provides coverage for $|\eta| < 3.2$. A steel-scintillator tile calorimeter provides hadronic energy measurements in the range $|\eta| < 1.7$. In the end-caps ($|\eta| > 1.5$), LAr hadronic calorimeters match the outer $|\eta|$ limits of the end-cap EM calorimeters. LAr forward calorimeters provide both EM and hadronic energy measurements, and extend the coverage to $|\eta| < 4.9$. Outside the calorimeters is an extensive muon spectrometer (MS) in a toroidal magnetic field, providing precise muon measurements within $|\eta| < 2.7$. The muon trigger system covers the range $|\eta| < 2.4$[39].

3.2.1 Object Definition

The key objects studied in this thesis are electrons, muons and missing transverse momentum. Information about these objects is gathered from various sub-detectors. A cross section of the various sub detectors is shown in Figure 3.4.

Electrons are reconstructed from energy deposits in the electromagnetic calorimeter matched to a track in the inner detector taking into account energy losses due to Bremsstrahlung. The four-momentum of the electrons is determined using the energy measurement from the calorimeter and the position measurement from the tracking detectors.

Muons are identified by tracks (or track segments) reconstructed in the muon spectrometer matched to tracks reconstructed in the inner detector. Their momenta are calculated by combining the information from the spectrometer, corrected for the energy loss in the calorimeter, with the inner detector track information.

Jets are reconstructed from topological clusters[41] using the anti-k_t algorithm[42] with radius parameter $R = 0.4$.

The E_T^{miss} is defined as the magnitude of the negative vector sum ($\vec{E}_T^{\text{miss}}$) of the p_T of muons, electrons, photons, jets and clusters of calorimeter cells not associated with these objects.

3.3 Physics with the upgraded ATLAS detector

The High Luminosity LHC (HL-LHC) is expected to begin collisions around 2024, with the aim of delivering an additional 2500 fb^{-1} to ATLAS over ten years, with total integrated luminosity of up to 3000 fb^{-1}[44]. The upgrades of the LHC will first see an intermediate stage: Phase-I, when the peak instantaneous luminosity will increase to 2.2×10^{34} cm^{-2}s^{-1} (around twice the nominal) and delivering around 300-400 fb^{-1} integrated luminosity by 2022.

The large luminosity extends the energy scales that can be studied in high energy boson-boson scattering, to study the EWSB mechanism, and to probe for signatures of new physics predicted by models such as SUSY and extra dimensions well into the multi-TeV region. In particular the reconstruction of complex SUSY cascade decays requires triggering and reconstruction of low p_T leptons and identification of heavy flavours.

The increased instantaneous luminosity at the HL-LHC results in the expected mean number of interactions per bunch crossing($<\mu>$) increasing from $<\mu>\sim 55$ at 2×10^{34} cm^{-2} s^{-1} to $<\mu>\sim 140$ at 5×10^{34} cm^{-2} s^{-1} (assuming a bunch crossing time of 25 ns) and the consequent increase in the integrated luminosity requires a detector able to operate after exposure to large particle fluences.

The ATLAS detector will be upgraded in preparation for the increases in beam luminosity. These changes tend to fall into roughly two categories. First there are changes to detector systems that are related to radiation damage. This comes either from the damage the existing systems will have already suffered or from the fact that these existing systems were not designed to accept the fluences that will result from HL-LHC. Secondly there are changes that are related to the increases in trigger rates and increased detector occupancy that comes about when large numbers of interactions occur within each beam crossing. The upgrades to the inner tracker (ITK) are largely being driven by the damage the detectors and system electronics will have suffered while the upgrades to the trigger and computer systems are driven by occupancy considerations[45].

The Phase-I upgrades will allow ATLAS to maintain low p_T trigger thresh-

olds for isolated leptons by increasing the granularity of the calorimeters involved in the Level-1 trigger and by introducing new muon trigger and tracking detectors in the forward direction. A new set of very far forward detectors will enable ATLAS to explore the new diffractive physics domain made accessible by the LHC energies and luminosities, providing sensitivity to large momentum transfer processes[46].

As for the Phase-II upgrades, the inner tracker will be replaced with a new all silicon tracker to maintain tracking performance in the high occupancy environment and to cope with the increase of approximately a factor of ten in the total radiation fluence. The LAr and Tile calorimeters and the Muon Spectrometer readout systems will be upgraded in order to cope with the high number of collisions per crossing. A new trigger architecture will be implemented exploiting the upgrades of the detector readout systems that will maintain and improve the event selection[44].

In order to fully understand the potential of the physics program with the upgraded ATLAS detector dedicated studies are required. We focus on prospects to search for SUSY signatures with di-leptons and missing energy. These searches will be simulated to match conditions for Phase-I and Phase-II HL-LHC.

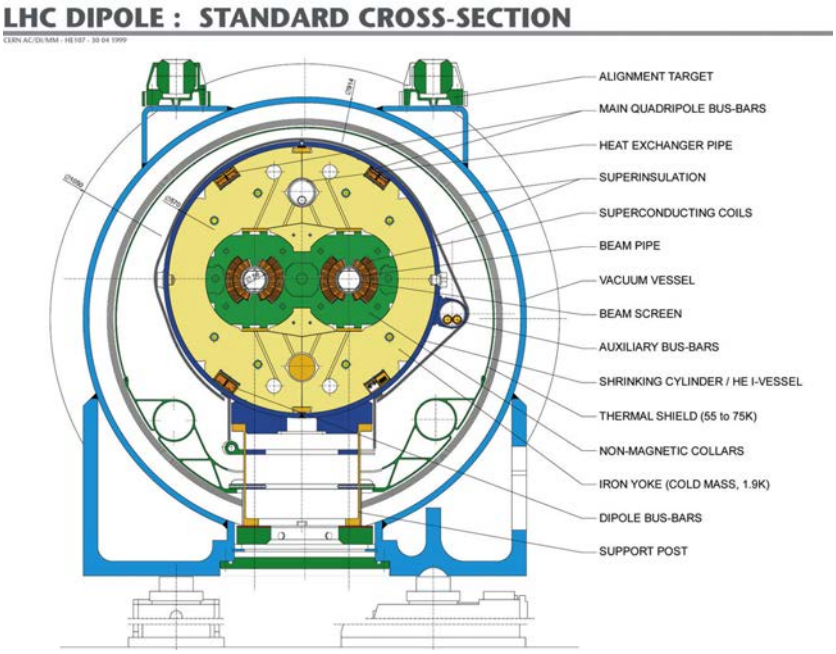

Figure 3.1: Cross section of the LHC dipole magnet [37]

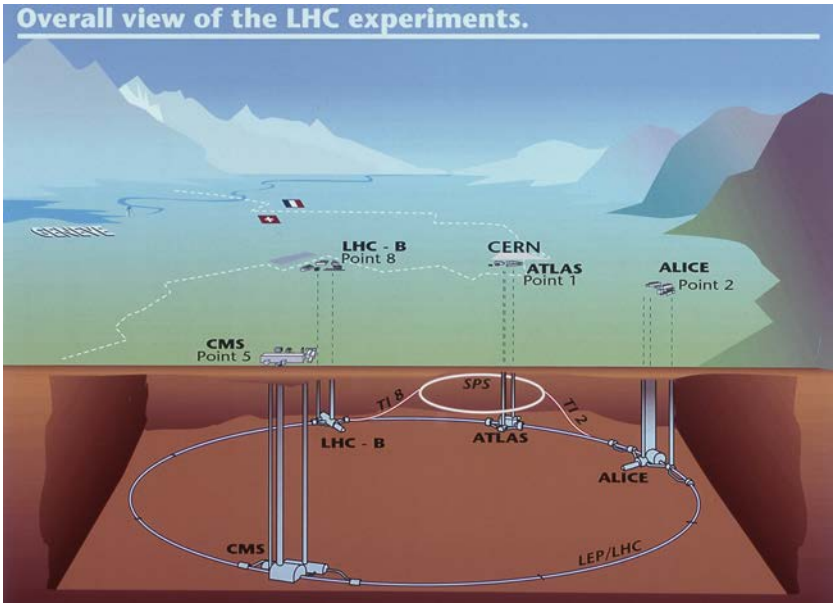

Figure 3.2: The LHC and various experiments [38]

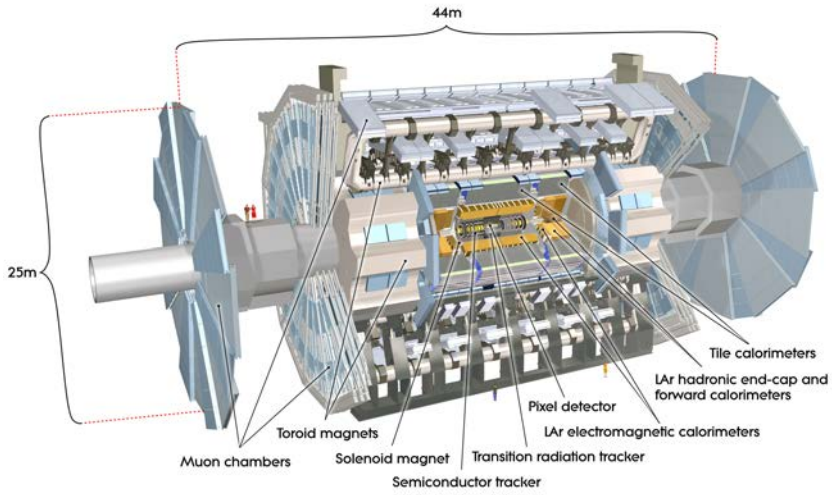

Figure 3.3: The ATLAS detector and its sub-detectors[40]

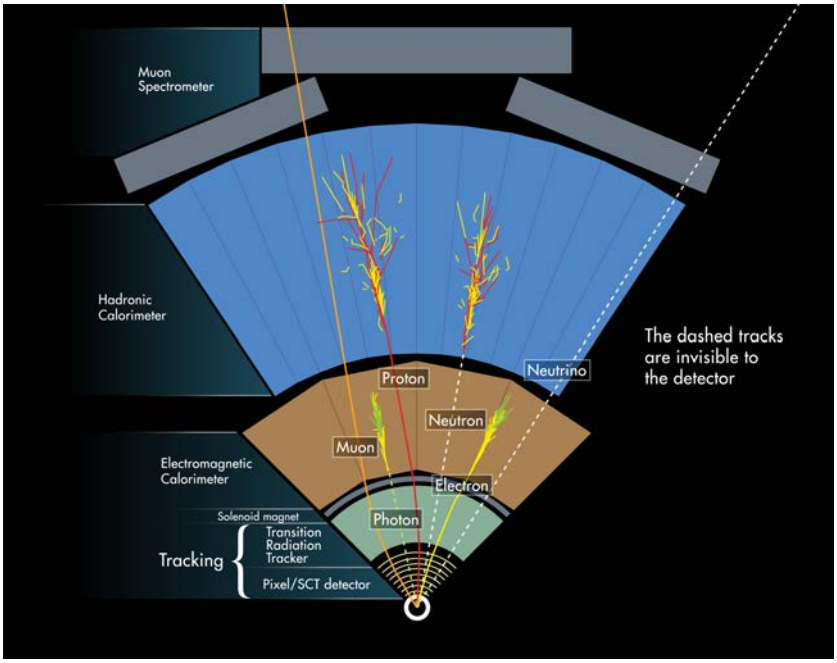

Figure 3.4: The various detectors sensitive to various particles [43]

Chapter 4

Kinematic Variables

Unless the particles are stable, we search for them through their decays. We will be expecting various other processes that will share this same final state topology as the process of interest. The events we search for are called the signal, and the other events which will also be picked up due to having the same final state are called the background. Since we cannot expect our process to have a unique signature in terms of particles the kinematics must also be considered.

Variables measured directly such as momenta of jets and leptons, angular differences between them and their masses can be used. From conservation of momenta we can also obtain the total momentum of the undetectable objects, the associated energy is called the missing transverse energy.

For discerning processes that will have very similar kinematics in terms of observable particles, we need to look for correlations between variables as well as constructing variables which have sensitivity to properties of the decay. Having sensitivity to unique properties becomes even more important when the events of interest have very small cross sections in comparison to the background events, as is the case for $\tilde{\ell}^+\tilde{\ell}^-$ production.

The CMS and ATLAS experiments have used the kinematic variables $M_{CT\perp}$[47, 48] and M_{T2}[49, 50] for searches of slepton and chargino pair production. These variables are designed to have sensitivity to the mass difference between the parent and invisible daughter particles. The M_{T2} variable uses the momenta of the visible particles, the missing transverse momenta and assumes a mass for the invisible outgoing particles. From the decay chain we expect two branches, we take the maximum transverse mass of the two branches and minimise it over the unknown split between the missing transverse momenta from each branch, this extremisation is M_{T2}. Over many events the maximum value of M_{T2} should give us the mass of the parent particle. The $M_{CT\perp}$ variable employs a contraint between the masses of parent

and child particles at various stages along the decay chain. If visible daughter particles are considered massless, and assuming a lack of initial state radiation, then it is bounded by:

$$M_{CT\perp}^{\max} = \frac{m^2(\delta) - m^2(\alpha)}{m(\delta)}, \tag{4.1}$$

[51] where $m(\delta)$ is the mass of the originally produced particle and $m(\alpha)$ is the mass of the invisible daughter of that decayed from δ. Unfortunately $M_{CT\perp}$,M_{T2} and the original formulation of the razor[52][53] variable, described in section 4.1, lose effectiveness when this mass difference is close to or smaller than the W mass.

The razor[52] variables described in section 4.1 also have this issue, which motivates us to construct the super razor variables, described in section 4.2. With the improved razor variables we would like to find any relevant mass differences that come as a result of electro-weak production [27].

4.1 Razor

Razor[52] variables were designed to search for new physics while allowing for some ambiguity. In this iteration we look to analyze pair production. From the collision, we obtain two particles labelled S_1 and S_2 both with a mass of m_s. We then expect these to decay into invisible and visible particles, which we label χ_i and Q_i respectively, where the i is either 1 or 2 depending on the parent particle. Both χ_i have a mass of m_χ.

In the rest frame of S_i, we can calculate the energy of Q_i using m_s and m_χ like so:

$$2E_1 = 2E_2 = \frac{m_s^2 - m_\chi^2}{m_s} \equiv M_\Delta, \tag{4.2}$$

where E_i is the energy of the visible Q_i in the rest frame of S_i .

Given that both decays are likely to create objects that are not detectable, it is impossible to accurately reconstruct these rest frames. However the razor approach gives an approximation that is reliable, on average, with some assumptions.

There are several frames which are of interest to the analysis of pair produced particles. The first is the lab frame, followed by the centre of mass (CM) frame of the pair produced particles, and then the two decay frames of S_1 and S_2.

We assume that S_i are made at near threshold energy level. We make a transformation from the lab frame to the razor frame R. This frame is

the approximation for the CM frame, where S_1 and S_2 are produced. The approximate boost we make from lab to R frame is labelled $\vec{\beta}_L$, the true boost from lab to CM is labelled $\vec{\beta}_{CM}$. The magnitude of $\vec{\beta}_L$ is defined as

$$\beta_L = \frac{q_1^z + q_2^z}{E_1 + E_2}, \tag{4.3}$$

where q_i^z is the longitudinal component of momenta of the Q_i particle.

In the CM frame, we expect the objects Q_1 and Q_2 to have equal and opposite z component of momentum, so in our R frame $2E_{R1} \approx 2E_{R2} \approx M_\Delta$. The longitudinal invariant mass term,

$$M_R^2 = (E_1 + E_2)^2 - (q_1^z + q_2^z)^2 \tag{4.4}$$

would then peak near M_Δ. However this only holds if, given enough statistics, the observable objects have opposite momenta and the initial objects are created near threshold.

Another mass variable is defined as

$$\left(M_T^R\right)^2 = \frac{1}{2}\left[E_T^{\text{miss}}\left(q_{1T} + q_{2T}\right) - \vec{E}_T^{\text{miss}} \cdot \left(\vec{q}_{1T} + \vec{q}_{2T}\right)\right] \tag{4.5}$$

which makes use of any missing transverse momenta in its calculation. Again, with our assumption of pair production at threshold energies, $M_t^R \leq M_R$. We can then define a ratio between these two mass variables

$$R^2 = \left(\frac{M_T^R}{M_R}\right)^2. \tag{4.6}$$

For backgrounds with very little E_T^{miss}, $R \sim 0$, and for signal events we expect a rough spread around $R^2 \sim \frac{1}{4}$.

Ideally these variables would distinguish pair production of heavy particles from QCD generated background events. In practice, all visible particles from an event are assumed to originate from a decay of the original S_1 or S_2 particles. As a result of this, all the visible momenta are summed into either Q_1 or Q_2, and the calculation is done as if there are only two visible objects.

4.2 Super Razor

Our first modification to the razor method is by assuming that a set of the visible particles are results of some initial state radiation or other source, not the decay of the heavy particle. Label the sum of these other particles 3-momentum $\vec{J}$. The transverse momentum of this is

$$\vec{J}_T = -\vec{E}_T^{\text{miss}} - \vec{q}_{1T} - \vec{q}_{2T}. \tag{4.7}$$

Armed with this we can transform to a more accurate approximation of the CM frame. From frame R, we need to make a transformation in the opposite direction of $\vec{J}$.

Unfortunately there is insufficient information to obtain the magnitude of the boost. The actual boost is

$$\vec{\beta}^{\mathrm{CM}} = \frac{\left\{-\vec{J}_T, p_Z^{\mathrm{CM}}\right\}}{\sqrt{|\vec{J}_T|^2 + \left(p_z^{\mathrm{CM}}\right)^2 + \hat{s}}} \tag{4.8}$$

where p_z^{CM} is the longitudinal momentum of the CM frame relative to the lab frame. The p_z^{CM} and $\hat{s}$ variables cannot be directly measured from the detectable particles, and hence have to be replaced with approximations.

To get to the razor frame R we make a boost in addition to $\vec{\beta}_L$, labelled $\vec{\beta}_R$. This transformation is defined

$$\vec{\beta}^{R} = \frac{\left\{-\vec{J}_T, p_Z^{R}\right\}}{\sqrt{|\vec{J}_T|^2 + |p_z^{R}|^2 + \hat{s}_R}} \tag{4.9}$$

where $\hat{s}_R$ is an approximation to the CM energy.

$\hat{s}_R$ is constructed under some assumptions, the first being that the invariant mass of the visible components is equal to the invariant mass of the invisible components, the second assumption is that the constructed variables are invariant under longitudinal boosts. The first assumption causes $\hat{s}_R$ to be an underestimate of $\hat{s}$ when the weakly interacting particles are massive. We can extremize[1] this underestimated variable by setting $p_Z^R = 0$. Hence, the transformation β_R is entirely transverse. Due to this construction, β_L will be the only transformation in the longitudinal direction. Despite the assumptions leading to values which are incorrect on an event by event basis, the variables that we construct in the R frame should still be invariant under the true longitudinal boosts.

4.2.1 Mass variables

The $\hat{s}_R$ variable can be defined using the variable defined in Equation 4.4,

$$\frac{\hat{s}_R}{4} = \frac{1}{2}\left(M_R^2 + \vec{J}_T \cdot (\vec{q}_1 + \vec{q}_2) + M_R\sqrt{M_R^2 + |\vec{J}_T|^2 + 2\vec{J}_T \cdot (\vec{q}_1 + \vec{q}_2)}\right). \tag{4.10}$$

This variable absorbs information about the original mass difference (M_Δ) and the total energy in the pair production ($\sqrt{\hat{s}}$). In the Razor framework,

[1]The word 'extremize' is used to include both minimize and maximize.

we interpret this mass variable as the energy associated with the boost to an approximation of the pair production frame.

From the Razor frame R we can make additional transformations to the rest frames to each of the produced particles S_i. Again we do not have sufficient information to make these transformations, so we must make do with an approximation. The two boosts are equal and opposite in direction to each other, the boost to S_1 being

$$\vec{\beta}_{R+1} = \frac{\vec{q}_{R1} - \vec{q}_{R2}}{E_{R1} + E_{R2}}. \tag{4.11}$$

where E_{Ri} is the energy of Q_i in the razor frame.

The invariant mass of the pair production frame would be related to the mass of the particle S_i by

$$\sqrt{\hat{s}} = 2\gamma^{decay} m_s \tag{4.12}$$

assuming we correctly identified $\vec{\beta}^{decay}$.

Given that we are constructing our boosts using the visible information from Q_i, we need our boost $\vec{\beta}_{R+1}$ and $\sqrt{\hat{s}_R}$ to be related to M_Δ instead of m_s. We define another mass variable

$$M_\Delta^R = \frac{\sqrt{\hat{s}_R}}{2\gamma_{R+1}} = \sqrt{\frac{4\left(q_1 \cdot M\right)\left(q_2 \cdot M\right) - m_{12}^4}{\hat{s}_R}} \tag{4.13}$$

where γ_{R+1} is the Lorentz factor associated with the boosts $\vec{\beta}_{R+1}$,m_{12} is the lepton pair invariant mass and the four-vector M is the missing transverse momentum (defined after the boost β_L) promoted to a four-vector with invariant mass of the di lepton system:

$$M \equiv \left(\sqrt{m_{12}^2 + |\not{\vec{E}}_T|^2}, \not{\vec{E}}_T\right). \tag{4.14}$$

These two variables $\hat{s}_R$ and M_Δ^R both estimate M_Δ, though they contain independent kinematic information in that estimation.

We would also like a variable that encapsulates information about the mass scale of the new particles, as opposed to M_Δ, this would be useful in the cases when the mass splitting is small or approaches that of the W boson. However, from this point in order to obtain more information we move onto angular variables.

4.2.2 Angular variables

The azimuthal angle between the razor boost $\vec{\beta}_R$ and the sum of visible momenta, $\vec{q}_1+\vec{q}_2$, calculated in the the razor frame R, inherits information about the ratio of masses of pair produced particles and their invisible daughters. This variable is labelled $\Delta\phi_R^\beta$. Its sensitivity to mass splitting arises from the assumption of the visible and invisible system having equal invariant mass. When $\hat{s}_R < \hat{s}$ then the boost $\vec{\beta}_R > \vec{\beta}^{CM}$. Due to the boost being larger, the visible momenta will be anti aligned with the boost direction. When $m_\chi/m_s \ll 1$, we would then expect $\Delta\phi_R^\beta$ to peak near π.

We can construct one more variable in the R frame. The variable $\sqrt{\hat{s}_R}$ can also be split into three components:

$$\frac{\sqrt{\hat{s}_R}}{4} = \left(M_\Delta^R\right)^2 + \left(q_{1R} + q_{2R}\right)^2 + \left(E_{1R} - E_{2R}\right)^2 . \tag{4.15}$$

Of these components, $E_{1R} - E_{2R}$, has not been used. This component has sensitivity to M_Δ, as with our other mass variables. We define a variable

$$|\cos\theta_{R+1}|^2 = \frac{\left(E_{1R} - E_{2R}\right)^2}{\hat{s}_R/4 - \left(M_\Delta^R\right)^2} \tag{4.16}$$

As the notation indicates, this variable can be interpreted as the cosine of the angle between the $\vec{\beta}_{R+1}$ boost and $\vec{q}_1$ or $\vec{q}_2$ in the $R+1$ frame.

Chapter 5

Event Generation, Simulation and Analysis Tools

5.1 Monte Carlo Generation and Analysis

Monte Carlo event generators are used to generate the data samples used in our analysis. They use Monte Carlo techniques to generate a set of data of events that would occur at collision. These generators are given certain rules to constrain the types of decays possible, and there are a wide variety of generators ideal for generating events of different processes.

From these event generators each event has information stored about the objects generated. This will typically include a list of the kinematics of leptons, jets and initial state radiation objects, as well as information relating to decay chains (i.e mother particles). At the truth level, all the relevant information is available. In order to do analysis from the perspective of a detector, where there will be misidentified objects, efficiency factors etc. simulation is required.

In the studies presented in this thesis the following data samples were produced using a few different generators. The Higgs vector boson fusion(VBF) and gluon fusion production were generated using POWHEG+PYTHIA8. POWHEG is used for the next-to-leading order (NLO) calculation, it produces events with positive(constant) weight and doesn't depend on the subsequent shower Monte Carlo program. It can also be easily interfaced to any modern shower generator, like PYTHIA8. Features such as tagging of parton lines and the tuning of the real cross section in POWHEG have been applied to deal with VBF Higgs boson production [54][55].

The $t\bar{t}$ and W^+W^- samples were generated with HERWIG+JIMMY [56] with the MC@NLO package[57]. HERWIG is a Fortran Monte Carlo pack-

age for simulating Hadron Emission Reactions With Interfering Gluons, and JIMMY is a library of routines which should be linked with the HERWIG. JIMMY can generate multiple parton scattering events in hadron-hadron, photon-photon or photon-hadron events. MC@NLO is a Monte Carlo generator that works like a regular Monte Carlo generator, but on top of that knows how to treat hard emissions, and can compute rates to NLO accuracy.

The Z+Jets and di-boson+Jets samples were generated using ALPGEN with HERWIG+JIMMY. ALPGEN is an event generator dedicated to the study of multiparton hard processes in hadronic collisions. The code performs, at the leading order in QCD and EW interactions, the calculation of the exact matrix elements for a large set of parton-level processes of interest in the study of the Tevatron and LHC data[58].

The SUSY signal samples were generated using HERWIG++ which is essentially HERWIG written in C++. This data is stored in n-tuples, where each ntuple is considered an event. The cross sections and efficiencies of the various datasets can be seen in Appendix A.

ROOT[59] is a framework of data analysis which was constructed by CERN. It relies on C++, and takes advantage of object oriented programming. It is used in the context of this thesis to apply a smearing to the truth values (with some extra packages) to simulate detector conditions and to perform the analysis of the data.

5.2 MET Smearing

The truth level objects will have to be parameterised to match performance of the experimental detectors. We parameterise the E_T^{miss} and b-tagging based off full simulation of the Phase-II ATLAS detector. The samples used in the parameterisation are $Z' \to t\bar{t}(m_{Z'} = 2$ TeV), minimum bias and di-jet all at $\sqrt{s} = 14$ TeV and 25 ns bunch spacing for a set of pile-up conditions. Matching the expected pileup mentioned in section 3.3, we use $< \mu >= 60$ for L=300fb^{-1} and $< \mu >= 140$ for L=3000fb^{-1}.

The true value of E_T^{miss} is smeared using a Gaussian function:

$$E_{x,y}^{\text{miss}} = E_{x,y}^{\text{miss,true}} + \text{Gaussian}(0, \sigma(\mu)), \tag{5.1}$$

where $\sigma(\mu)$ is the resolution which depends on the average number of pileup events.

The resolution of E_T^{miss} depends on $\sum E_T$, which is the sum of the true value of $\sum E_T$ and the $\sum E_T$ due to pileup (labelled $\sum E_T^{\text{PU}}$). We can then define:

$$\sum E_T^{\text{PU}} = \sum E_T - \sum E_T^{\text{True}}. \tag{5.2}$$

Figure 5.1 shows the distribution of E_T^{PU} for the Z' and minimum bias samples. A random value from the E_T^{PU} distribution is added to E_T^{True} to obtain an estimate of E_T. Figure 5.2 shows the reconstructed distribution of E_T^{miss} compared to parametrisations previously used for inputs to the European Strategy group [60].

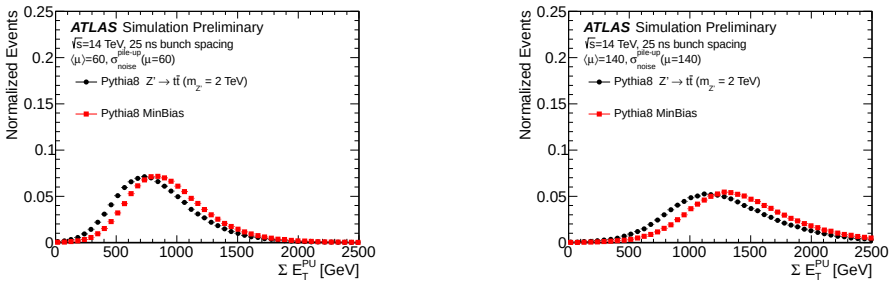

Figure 5.1: $\sum E_T^{PU}$ distribution for $<\mu>=60$(left) & $<\mu>=140$ (right)[60].

5.3 Event reconstruction

After event samples are generated from Monte Carlo generators, we attempt to construct the event, and select objects which are likely results of the collision. Since our generated data also generates initial state radiation, we need to make a selection from the list of jets, electrons and muons. The first criteria of selection is a momentum threshold. Electrons and jets are selected with a $p_T > 20$ GeV. Muons are selected with a $p_T > 5$ GeV. The next step is to apply an efficiency map, which smear the transverse momenta of the selected objects. The E_T^{miss} here is also smeared in conjunction with the objects. The smearing here allows for better simulation of artifacts from experimental pile-up.

We also need to check if jets are overlapping with electrons or faking electrons. If the quantity:

$$\Delta R = \sqrt{\Delta\eta^2 + \Delta\phi^2}, \tag{5.3}$$

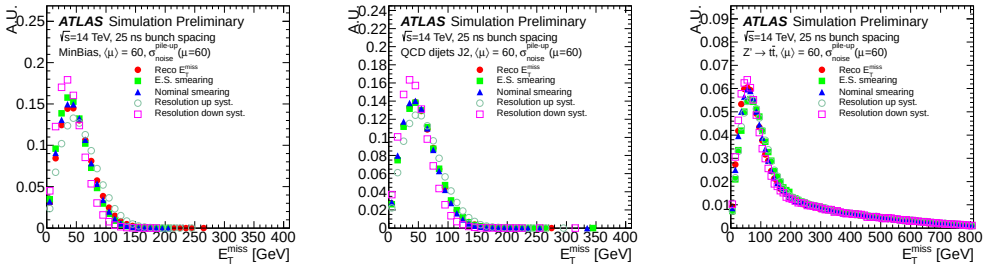

Figure 5.2: E_T^{miss} distribution for $< \mu >= 60$ obtained from the parametrisation (blue) and compared to the reconstructed value obtained from full simulation (red) and to the parametrisation used for the European Strategy. (green).The closure of the parametrisation is tested in different physics processes: from left to right, minimum bias, di-jet and Z' events. Systematic variations are also included (open markers) and shown to cover the differences between the parametrisation and the reconstructed E_T^{miss}[60].

where $\Delta\eta$ and $\Delta\phi$ are the two angular differences between the jet and the electron, is less than 0.2, we need to check if the jet is faking an electron using another efficiency map. The object is then labelled as an electron if it passes this criteria. The objects labelled electrons are then checked for overlap with jets. ΔR is used again for this check, if the value is less than 0.4 with any of the jets, then the electron object is discarded.

After this process we have a list of jets, electrons and muons and their four momenta in the lab frame for each event.

Chapter 6

Results and Interpretation

6.1 Event Selection

From the list of objects we find the two highest momentum leptons, taken from the list of muons and electrons. We discard events which do not have exactly two leptons from any analysis with the super razor variables.

In the di-slepton analysis we consider the cases when the two leptons are of the same flavour, opposite charge, as our final states are e^+e^-,$\mu^+\mu^-$ produced in association with missing energy. The leading lepton is required to have $p_T > 35$ GeV, the sub leading lepton is required to have $p_T > 20$ GeV.

In the di-chargino analysis, events are selected where the two leptons have different flavours. While leptons of the same flavour are equally possible from the decay of the di-chargino pair, this strict requirement eliminates backgrounds from real Z decays (either to e^+e^- or $\mu^+\mu^-$) while still retaining $\approx 20\%$ efficiency for signal production.

6.2 Di-slepton production

6.2.1 Analysis for Phase-I: $300\mathbf{fb}^{-1}$ with $< \mu >= 60$

Figures 6.1 - 6.13 show histograms of kinematic variables with the same flavour selection as mentioned in section 6.1, with the events scaled to 300 fb^{-1} and expected mean number of interactions per bunch crossing $< \mu >= 60$. Any events that correspond to values larger than the range of the histograms are added to a final overflow bin. Two di-slepton production processes have been compared with the selected SM backgrounds, the masses of the sleptons are at 300 and 500 GeV, with massless neutralinos.

Figure 6.1 shows the M_{Δ}^{R} variable with and without a selection at 80 GeV. The signal samples have events that populate larger values of this variable, the mass difference between the slepton and neutralino produces an edge in the distribution. In the region above 80 GeV there are few Higgs and Z+jets background events. The WZ/ZZ+jets background events populate the same regions as the signal, making it somewhat problematic. A distribution of the masses of the leptons could be used to determine whether these leptons are predominantly arising from on-shell or off-shell Z bosons.

Table 6.1 shows the effect of various selection criteria on M_{Δ}^{R} on the selected background and signal samples, with Table 6.2 showing the relative effect of these selections in percentage. While these criteria are relatively efficient at maintaining the signal with elimination of background, the amount of events remaining is still quite low. With the last selection on M_{Δ}^{R}, there are around 70 to 350 signal events remaining and around 210 background events.

$\sqrt{\hat{s}}_{R}$ is displayed in Figures 6.2 and 6.3, with no selection on M_{Δ}^{R} and the $M_{\Delta}^{R} > 80$ GeV selection in Figure 6.2 and the selections $M_{\Delta}^{R} > 150$ GeV and $M_{\Delta}^{R} > 200$ GeV in in Figure 6.3. The distributions peak at approximately the combined masses of the parent particles, for instance, the Higgs background peaks near 125 GeV and the signals peak near the mass of the pair sleptons. However in the instances where the invisible system becomes massive, the peak underestimates the mass of the parent system. Higgs background does not have events past 700 GeV with no restriction on M_{Δ}^{R}. The selections on M_{Δ}^{R} eliminates events with $\sqrt{\hat{s}}_{R}$ being lower than twice the lowest value of M_{Δ}^{R}, as well as removing background events at the tail end of the distribution. By increasing the threshold of the M_{Δ}^{R} selection, the signal rises above the background for larger values of $\sqrt{\hat{s}}_{R}$.

The angular variable $\cos\theta_{R+1}$ is displayed in Figure 6.4, with and without the $M_{\Delta}^{R} > 80$ GeV selection. The signal events populate the lower values of $\cos\theta_{R+1}$, with a linear descent towards 1. The Z+jets background events also populate the lower values, but with a more significant drop towards 1. The removal of the Z+jets background from the first selection causes a significant change in shape of the background, with similar shape to that of the signal, though still larger than the signal. The remaining selections for this variable can be seen in Figure 6.5, the di-boson backgrounds still being difficult to separate from the signal.

The angle $\Delta\phi_{R}^{\beta}$ is displayed in Figure 6.6, with and without the $M_{\Delta}^{R} > 80$ GeV selection. The first selection reduces the discrepancy in background and signal with a complete removal of Higgs background in the region $\Delta\phi_{R}^{\beta} < 1.5$. The larger selections are displayed in Figure 6.7, the remaining signal events and di-boson background are spread over all the values of this variable.

The angle between the two leptons in the R-frame is described in Figures 6.8 and 6.9. The Z+jets background has the most significant impact on the shape of the background, featuring a distinct rise in events for values above 1. The signal has a rise in events toward π. The first selection on M_{Δ}^{R} restricts the Higgs background to values less than 1.5 and causes a significant drop in background events near π. The signal also receives a dip near π, but they have the least discrepancy to the background near 2.75. The remaining selections, shown in Figure 6.9, can separate the signal from the di-boson background in the region $\Delta\phi_{l_1,l_2} > 1$.

The angle between the two Super Razor frames is shown in the Figures 6.10 and 6.11. With no selections, both background and signal appear to be spread evenly across all values of this variable. As with the other angular variables the relative reduction in Higgs and Z+jets background has the most noticeable effect with the first selection on M_{Δ}^{R}. In a similar fashion to all the other angular variables (except $\Delta\phi_{l_1,l_2}$), the later selections leave a di-boson background spread almost evenly across the all values in a similar fashion to the slepton signals, but also at the same order.

The Lorentz factors for the super razor boosts are shown in Figures 6.12 and 6.13. The first transformation features the majority of both signal and background events with factors near 1, the second transformation features background and signal events with larger factors. A selection could be made to select events where $\gamma_{R+1} < 50$, as the tail end of both signal ends near there. The events with larger factors are removed with selections on M_{Δ}^{R}, they do not allow for distinguishing of signal from background.

As we make progressively tighter selections Monte Carlo statistics becomes an increasing concern. In particular, this analysis, and subsequent selections outlined in this thesis, suffers from low $t\bar{t}$ background. However, the shape and yield of these events, in the di-slepton selection would be modelled using an opposite flavour sample.

Table 6.1: Number of events passing each selection for each sample. No selection is just the initial event selection described in section 5.3. "slep selec" is the selection on the lepton p_T and flavour described in section 6.1. s_Mx is the selection $M_\Delta^R > x$ GeV.

selection	Higgs	$t\bar{t}$	W^+W^-	$Z(ll)$+jets	WZ/ZZ +jets	$(\mathrm{m}\tilde{\chi}_1^0, \mathrm{m}\tilde{l}_1) = (0, 500)GeV$	$(\mathrm{m}\tilde{\chi}_1^0, \mathrm{m}\tilde{l}_1) = (0, 300)GeV$
No selection	48416 ± 61	1976.0e+04 ± 1.4e+04	958690 ± 880	5629.3e+05 ± 2.0e+05	729340 ± 960	326.3 ± 5.4	2657 ± 23
slep selec	3205 ± 16	21840 ± 480	208850 ± 410	2965.2e+05 ± 1.5e+05	42100 ± 200	111.7 ± 3.2	1066 ± 14
s_M80	93.9 ± 2.8	3110 ± 180	12600 ± 100	3730 ± 510	4330 ± 63	100 ± 3	844 ± 13
s_M150	1.46e-02 ± 1.5e-02	74 ± 28	32.6 ± 5.2	0 ± 0	578 ± 22	83.9 ± 2.7	560 ± 10
s_M200	0 ± 0	21 ± 15	4.1 ± 1.8	0 ± 0	185 ± 13	70.7 ± 2.5	349.2 ± 8.2

Table 6.2: The percentage of surviving events from the slepton production signals with the selections described in table 6.1 rounded to two decimal places.

selection	$(\mathrm{m}\tilde{\chi}_1^0, \mathrm{m}\tilde{l}_1) = (0, 500)GeV$	$(\mathrm{m}\tilde{\chi}_1^0, \mathrm{m}\tilde{l}_1) = (0, 300)GeV$
No selection	100	100
slep selec	34.21	40.13
s_M80	30.66	31.77
s_M150	25.70	20.97
s_M200	21.63	13.14

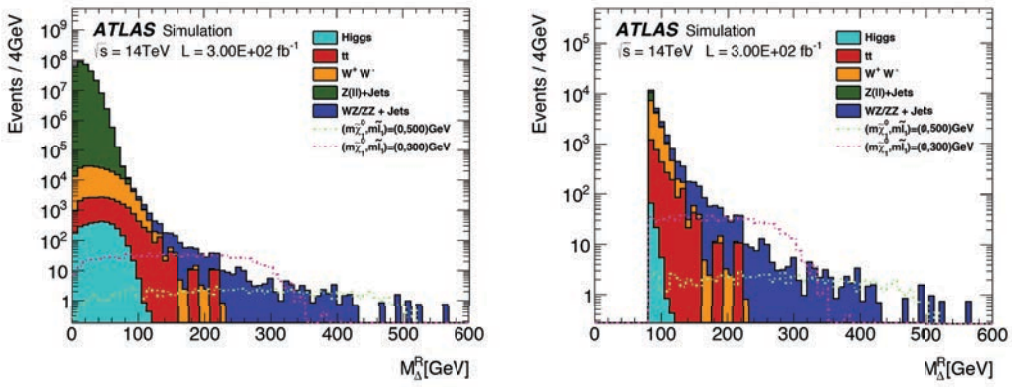

Figure 6.1: M_Δ^R for di-slepton production with selected SM backgrounds scaled to 300 fb^{-1} with $< \mu >= 60$. No selection (left) and a selection at $M_\Delta^R > 80$ GeV(right) are shown.

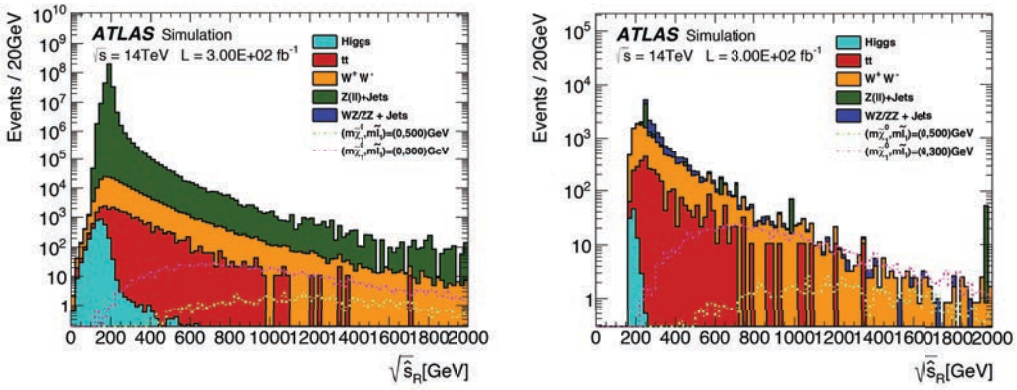

Figure 6.2: $\sqrt{\hat{s}_R}$ for di-slepton production with selected SM backgrounds scaled to 300 fb^{-1} with $< \mu >= 60$. No selection(left) and $M_\Delta^R > 80$ GeV(right) are shown.

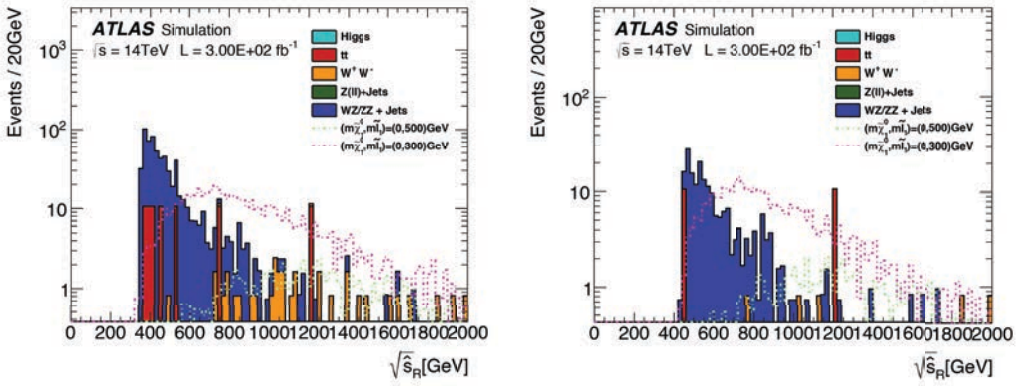

Figure 6.3: $\sqrt{\hat{s}_R}$ for di-slepton production with selected SM backgrounds scaled to 300 fb^{-1} with $< \mu >= 60$. The selections $M_\Delta^R > 150$ GeV(left) and $M_\Delta^R > 200$ GeV(right) are shown.

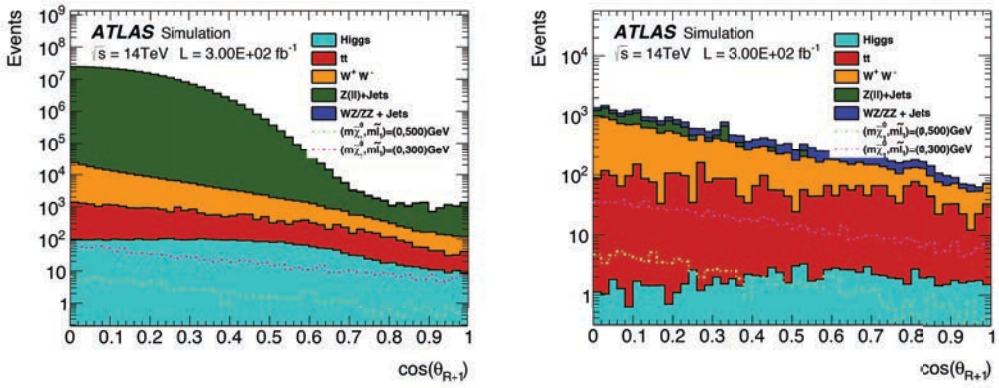

Figure 6.4: $\cos\theta_{R+1}$ for di-slepton production with selected SM backgrounds scaled to 300 fb^{-1} with $< \mu >= 60$. No selection(left) and $M_{\Delta}^{R} > 80$ GeV(right) are shown.

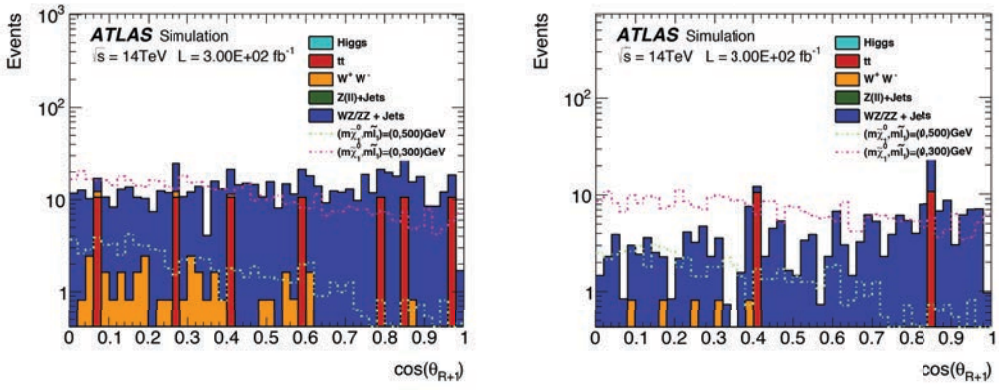

Figure 6.5: $\cos\theta_{R+1}$ for di-slepton production with selected SM backgrounds scaled to 300 fb^{-1} with $< \mu >= 60$. The selections $M_{\Delta}^{R} > 150$ GeV(left) and $M_{\Delta}^{R} > 200$ GeV(right) are shown.

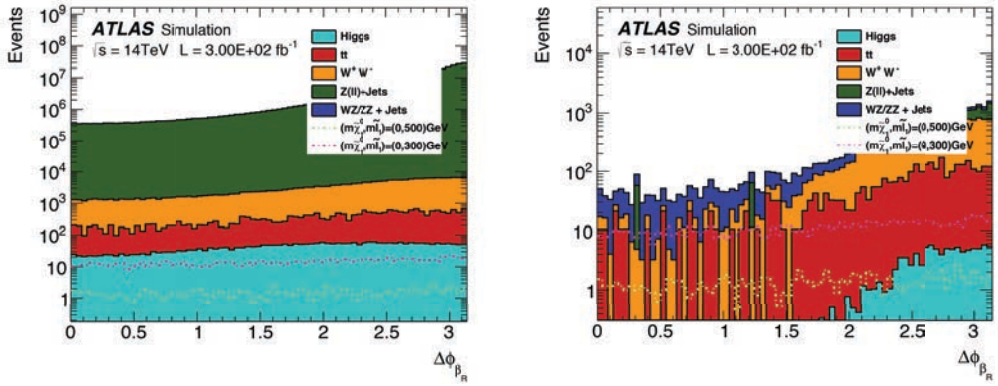

Figure 6.6: $\Delta\phi_R^\beta$ for di-slepton production with selected SM backgrounds scaled to 300 fb^{-1} with $< \mu >= 60$. No selection(left) and $M_\Delta^R > 80$ GeV(right) are shown.

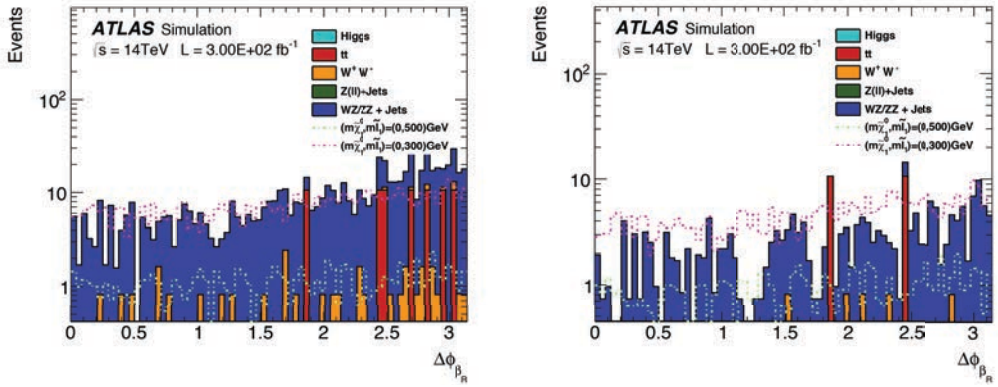

Figure 6.7: $\Delta\phi_R^\beta$ for di-slepton production with selected SM backgrounds scaled to 300 fb^{-1} with $< \mu >= 60$. The selections $M_\Delta^R > 150$ GeV(left) and $M_\Delta^R > 200$ GeV(right) are shown.

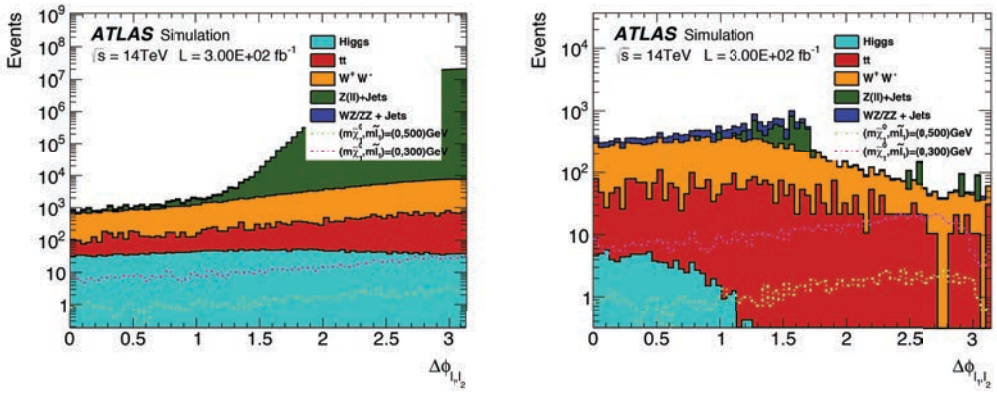

Figure 6.8: $\Delta\phi_{l_1,l_2}$ for di-slepton production with selected SM backgrounds scaled to 300 fb^{-1} with $< \mu >= 60$, no selection(left) and $M_\Delta^R > 80$ GeV(right).

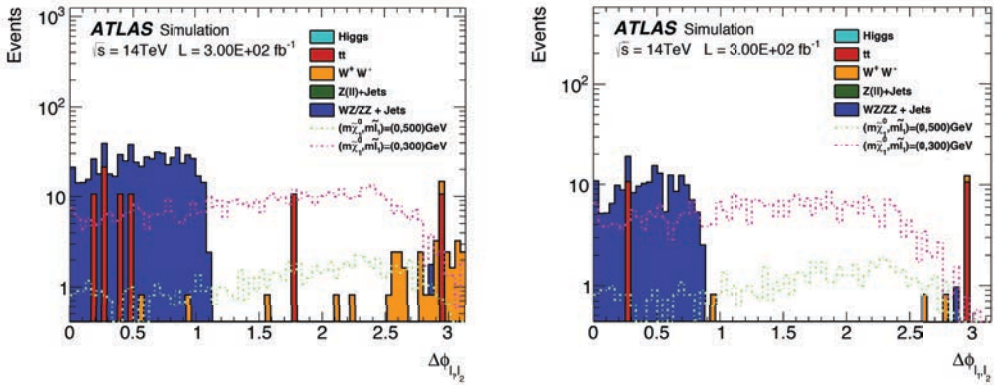

Figure 6.9: $\Delta\phi_{l_1,l_2}$ for di-slepton production with selected SM backgrounds scaled to 300 fb^{-1} with $< \mu >= 60$, the selection $M_\Delta^R > 150$ GeV(left) and $M_\Delta^R > 200$ GeV(right).

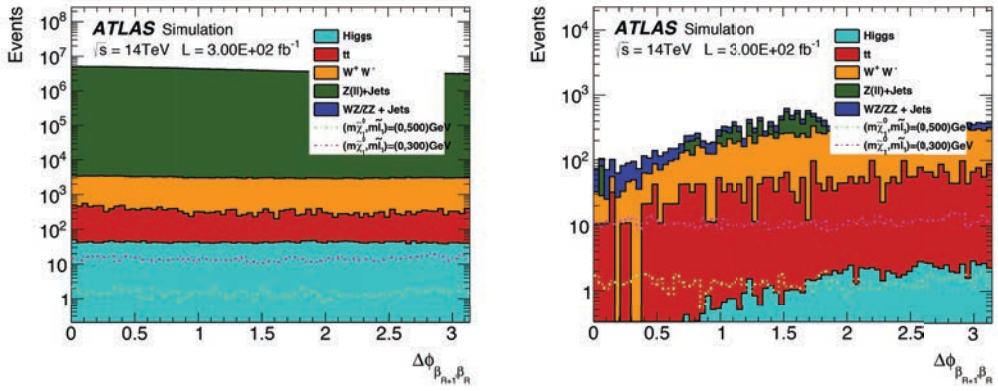

Figure 6.10: $\Delta\phi_\beta^{R+1,R}$ for di-slepton production with selected SM backgrounds scaled to 300 fb^{-1} with $< \mu >= 60$, no selection(left) and $M_\Delta^R > 80$ GeV(right).

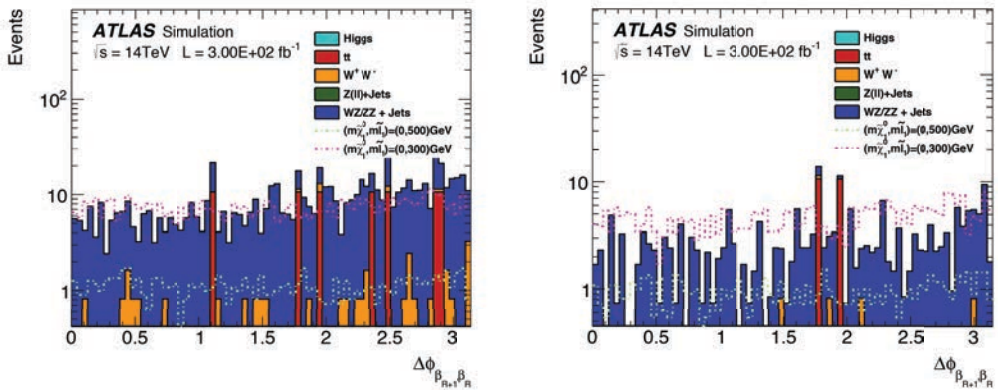

Figure 6.11: $\Delta\phi_\beta^{R+1,R}$ for di-slepton production with selected SM backgrounds scaled to 300 fb^{-1} with $< \mu >= 60$, the selection $M_\Delta^R > 150$ GeV(left) and $M_\Delta^R > 200$ GeV(right).

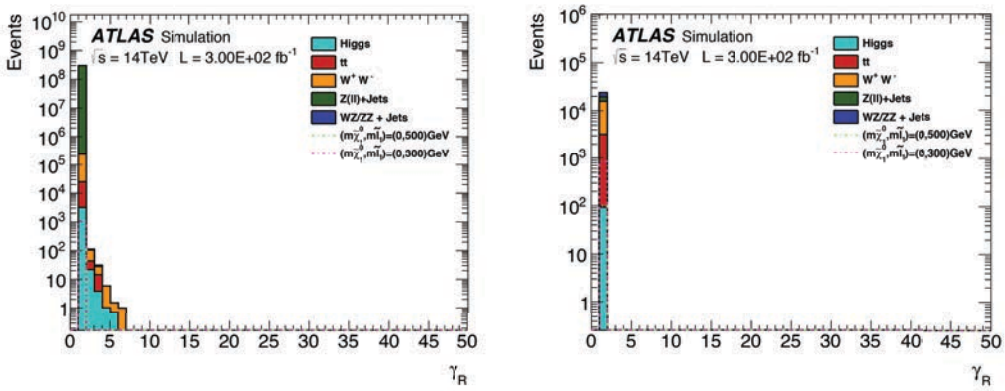

Figure 6.12: γ_R for di-slepton production with selected SM backgrounds scaled to 300 fb^{-1} with $< \mu >= 60$, no selection(left) and $M_\Delta^R > 80$ GeV(right).

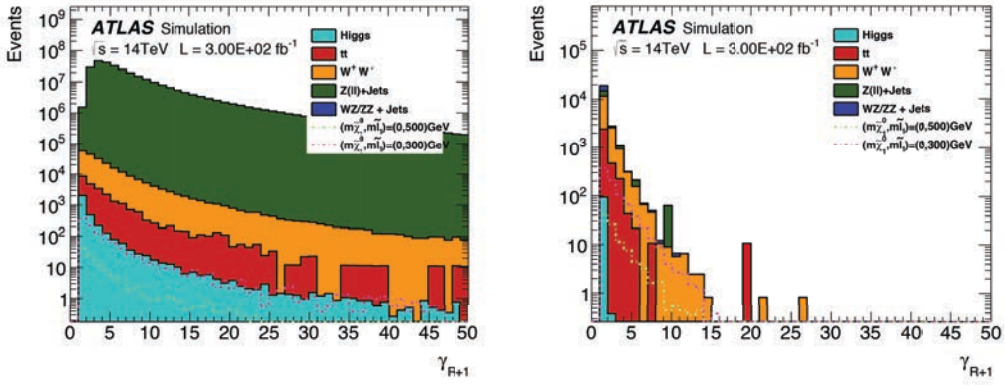

Figure 6.13: γ_{R+1} for di-slepton production with selected SM backgrounds scaled to 300 fb^{-1} with $< \mu >= 60$, no selection(left) and $M_\Delta^R > 80$ GeV(right).

6.2.2 Analysis for Phase-II: 3000fb^{-1} with $<\mu>=140$

For the Phase-II analysis, the histograms are scaled to 3000 fb^{-1}, with expected mean number of interactions per bunch crossing $<\mu>=140$ to match the detector conditions with the same event selection as in the Phase-I analysis.

The M_{Δ}^{R} distribution can be seen in Figure 6.14. We make selections at $M_{\Delta}^{R} > 80$ GeV, $M_{\Delta}^{R} > 150$ GeV and $M_{\Delta}^{R} > 200$ GeV. Figure 6.15 shows the events that are remaining with the $M_{\Delta}^{R} > 80$ GeV and $M_{\Delta}^{R} > 200$ GeV selections.

Table 6.3 shows the number of events that pass each selection, and Table 6.4 shows these in percentage ratios to the initial event selection. At this luminosity we yield both signal and background events around an order higher than the Phase-I analysis. With the last selection on M_{Δ}^{R}, there are around 700 to 3500 signal events remaining and around 2400 background events.

The variable $\sqrt{\hat{s}}_R$ is show in Figure 6.16. This variable should peak at an estimate of $\hat{s}$, but it comes with a large tail. The slepton production signal has the least discrepancy to the background in the higher energy regions, as demonstrated in Figures 6.17 and 6.18. The $M_{\Delta}^{R} > x$ GeV selection removes events where $\sqrt{\hat{s}}_R > 2x$ GeV, as well as reducing the background relative to the signal at the higher values of $\sqrt{\hat{s}}_R$.

There are some interesting correlations with M_{Δ}^{R} values and the angular variables. Figure 6.19 shows how the events from the Z+jets in $\cos\theta_{R+1}$ can be removed with a selection on M_{Δ}^{R}. The histograms with the other selections are shown in Figure 6.20, which features a persistence of the diboson background with similar appearance on the same order of the slepton production signals.

Figure 6.21 shows $\Delta\phi_R^{\beta}$ variable, the difference in azimuthal angle between the visible system and the boost β_R. The background distribution rises towards π, while the slepton production signal distribution appears flat. The first selection causes a significant reduction in discrepancy between the signal and background in the region of $\Delta\phi_R^{\beta} < 1.5$. The more stricter selections cause the background to level out to the same magnitude as the 300 GeV di-slepton production signal as can be seen in Figure 6.22.

The histograms of the angle between the two selected leptons in the R-frame $\Delta\phi_{l_1,l_2}$ can be seen in Figures 6.23 and 6.24. Without any selections, The Z+jets background has a large amount of its events in the region $\Delta\phi_{l_1,l_2} > 1$, whereas the remaining background and signal distributions have a rise towards π. The M_{Δ}^{R} selection has a dramatic effect on the shape of the Higgs and Z+jets background with a removal of events with large $\Delta\phi_{l_1,l_2}$.

The remaining selections allow for the signal to be seen above the background in the region $\Delta\phi_{l_1,l_2} > 1$.

The histogram of the angle between the two Super Razor frames, $\Delta\phi_\beta^{R+1,R}$, is shown in Figure 6.25 and Figure 6.26. With no selections, the distribution of signal and background are flat. The selections on M_Δ^R remove events with low $\Delta\phi_\beta^{R+1,R}$ in the background distribution, however the WZ/ZZ+jets background still mimics the signal distribution even with larger selections on M_Δ^R.

The Lorentz factors for the Super Razor boosts are shown in Figures 6.27 and 6.28. The boost to the $R+1$ frame features events with much larger factors than the R boost. The larger factors are associated with the lower values of M_Δ^R, and hence are removed with the selections. The signal and background don't have any distinguishing features in these variables.

Table 6.3: Number of events passing each selection for each sample. No selection is just the initial event selection described in section 5.3. s_cut is the selection on the lepton p_T described in section 6.1. s_Mx is the selection $M_\Delta^R > x$ GeV.

selection	Higgs	$t\bar{t}$	W^+W^-	$Z(ll)$+jets	WZ/ZZ +jets	$(\mathrm{m}\tilde{\chi}_1^0, \mathrm{m}\tilde{l}_1) = (0, 500)GeV$	$(\mathrm{m}\tilde{\chi}_1^0, \mathrm{m}\tilde{l}_1) = (0, 300)GeV$
No selection	458260 ± 610	2388.0e+05 ± 1.6e+05	9591.5e+03 ± 8.8e+03	5620.8e+06 ± 2.0e+06	7293.4e+03 ± 9.6e+03	3261 ± 54	26570 ± 230
slep selec	31850 ± 160	173.0e+03± 4.3e+03	2088.5e+03 ± 4.1e+03	2963.2e+06 ± 1.5e+06	421000 ± 2000	1116 ± 32	10670 ± 140
s_M80	2950 ± 50	31.4e+03 ± 1.8e+03	237.5e+03 ± 1.4e+03	366.2e+04 ± 5.3e+04	54930 ± 710	1000 ± 30	8420 ± 130
s_M150	0 ± 0	960 ± 320	725 ± 77	0 ± 0	6520 ± 240	833 ± 27	5620 ± 100
s_M200	0 ± 0	320 ± 180	65 ± 23	0 ± 0	2030 ± 130	703 ± 25	3530 ± 82

Table 6.4: The percentage of surviving events in the signal samples, with the same selections specified in Table 6.3, in respect to the events that pass the initial selection criteria.

selection	$(\mathrm{m}\tilde{\chi}_1^0, \mathrm{m}\tilde{l}_1) = (0, 500)GeV$	$(\mathrm{m}\tilde{\chi}_1^0, \mathrm{m}\tilde{l}_1) = (0, 300)GeV$
No selection	100	100
slep selec	34.21	40.13
s_M80	30.66	31.68
s_M150	25.48	21.14
s_M200	21.52	13.29

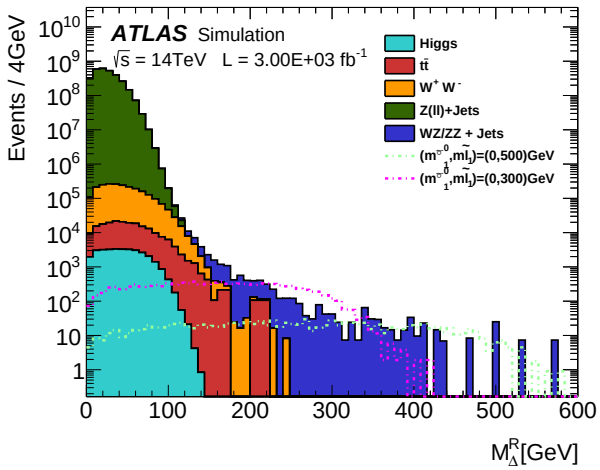

Figure 6.14: M_Δ^R for di-slepton production with selected SM backgrounds scaled to 3000 fb^{-1} with $< \mu >= 140$.

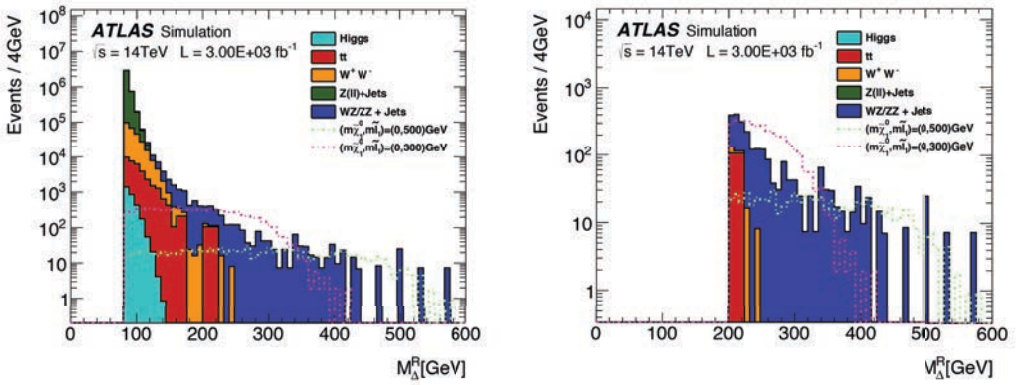

Figure 6.15: M_Δ^R for di-slepton production with selected SM backgrounds scaled to 3000 fb^{-1} with $< \mu >= 140$, selection at 80 GeV(left) and 200 GeV(right).

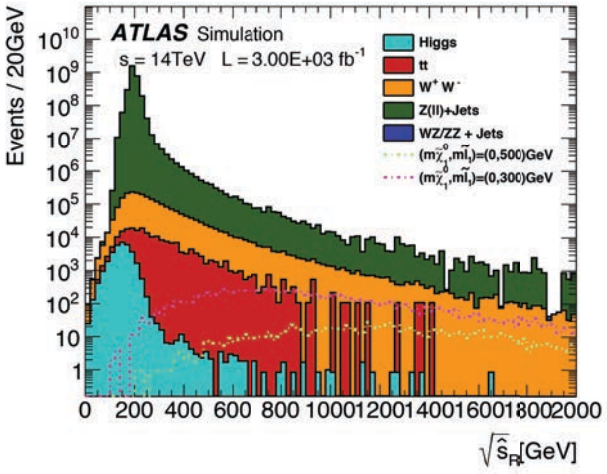

Figure 6.16: $\sqrt{\hat{s}}_R$ for di-slepton production with selected SM backgrounds scaled to 3000 fb^{-1} with $< \mu >= 140$.

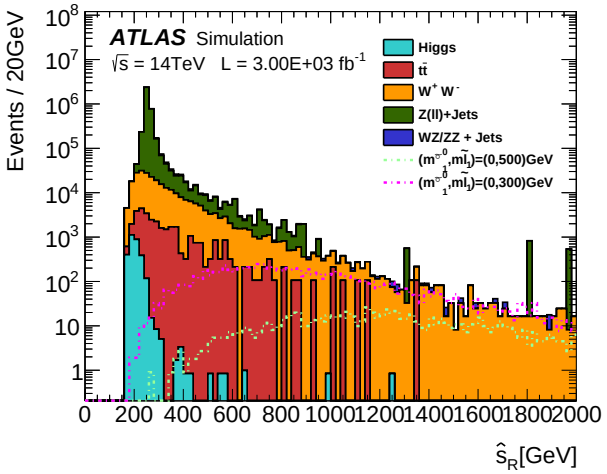

Figure 6.17: $\sqrt{\hat{s}}_R$ for di-slepton production with selected SM backgrounds scaled to 3000 fb^{-1} with $< \mu >= 140$ and selection $M_\Delta^R > 80$ GeV.

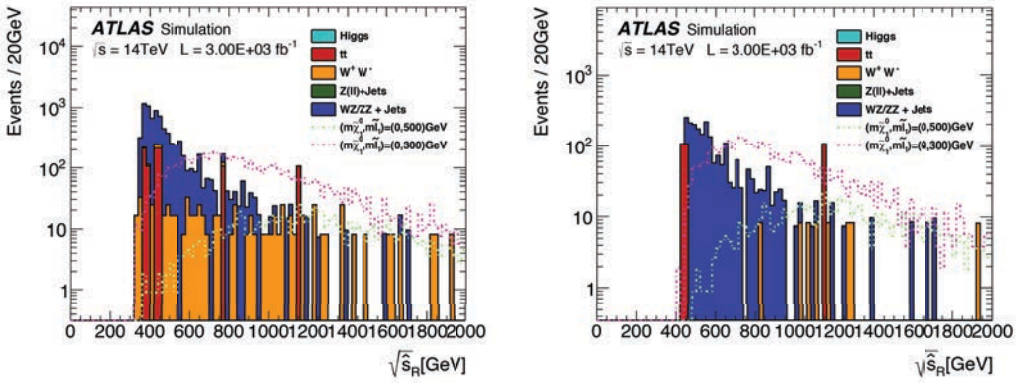

Figure 6.18: $\sqrt{\hat{s}_R}$ for di-slepton production with selected SM backgrounds scaled to 3000 fb^{-1} with $< \mu >= 140$, with selections $M_\Delta^R > 150$ GeV(left) and $M_\Delta^R > 200$ GeV(right).

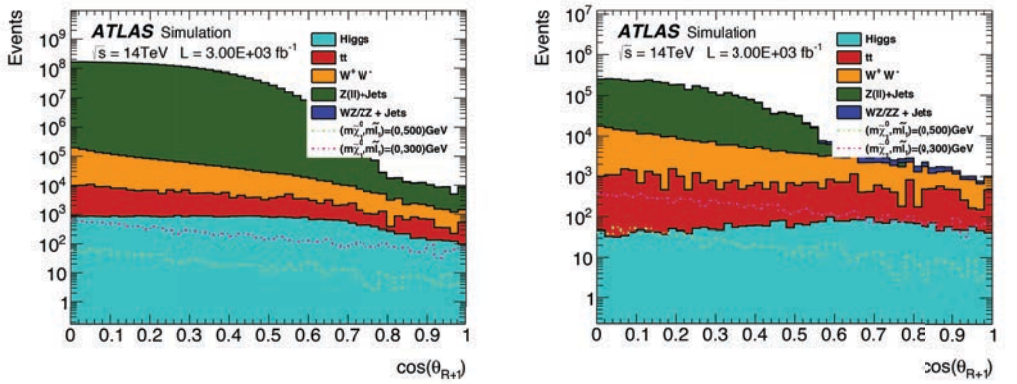

Figure 6.19: cosθ_{R+1} for di-slepton production with selected SM backgrounds scaled to 3000 fb^{-1} with $< \mu >= 140$, with no selection(left) and $M_\Delta^R > 80$ GeV(right).

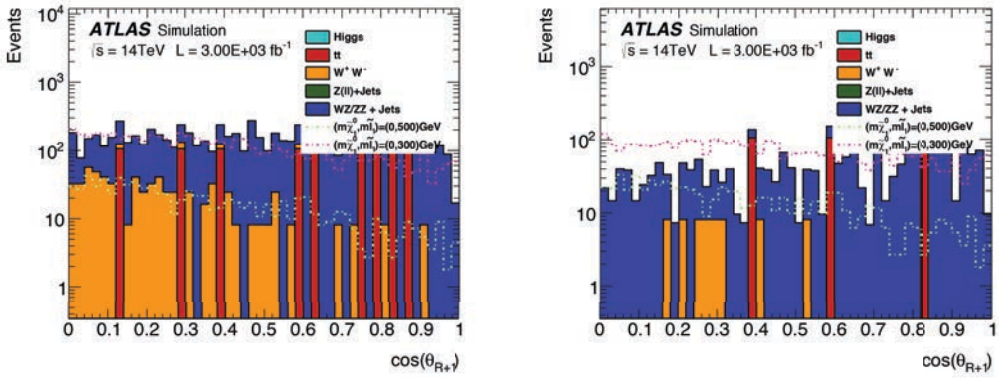

Figure 6.20: Again, $\cos\theta_{R+1}$ for di-slepton production with selected SM backgrounds scaled to 3000 fb^{-1} with $< \mu >= 140$, with selections $M_{\Delta}^{R} > 150$ GeV(left) and $M_{\Delta}^{R} > 200$ GeV(right).

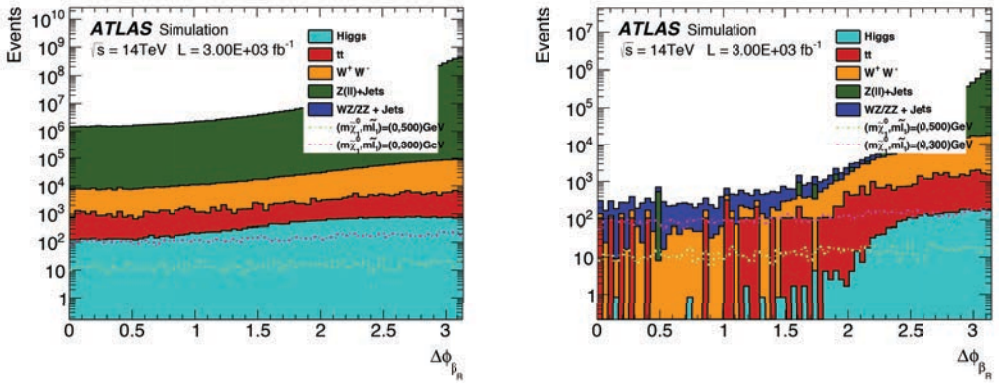

Figure 6.21: $\Delta\phi_{R}^{\beta}$ for di-slepton production with selected SM backgrounds scaled to 3000 fb^{-1} with $< \mu >= 140$, with no selection(left) and $M_{\Delta}^{R} > 80$ GeV(right).

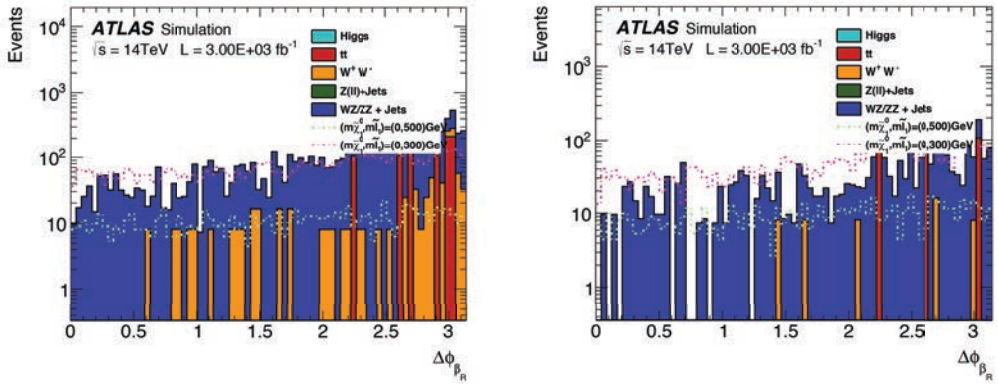

Figure 6.22: $\Delta\phi_R^\beta$ for di-slepton production with selected SM backgrounds scaled to 3000 fb^{-1} with $< \mu >= 140$, with selections $M_\Delta^R > 150$ GeV(left) and $M_\Delta^R > 200$ GeV(right).

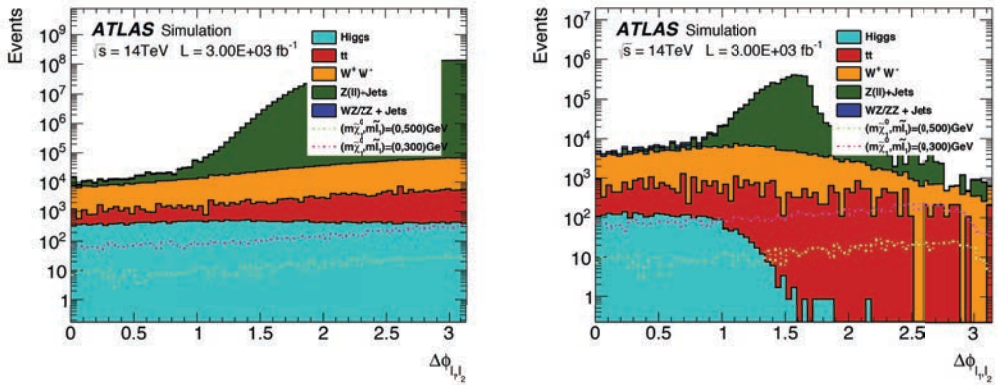

Figure 6.23: $\Delta\phi_{l_1,l_2}$ for di-slepton production with selected SM backgrounds scaled to 3000 fb^{-1} with $< \mu >= 140$, with no selection(left) and $M_\Delta^R > 80$ GeV(right).

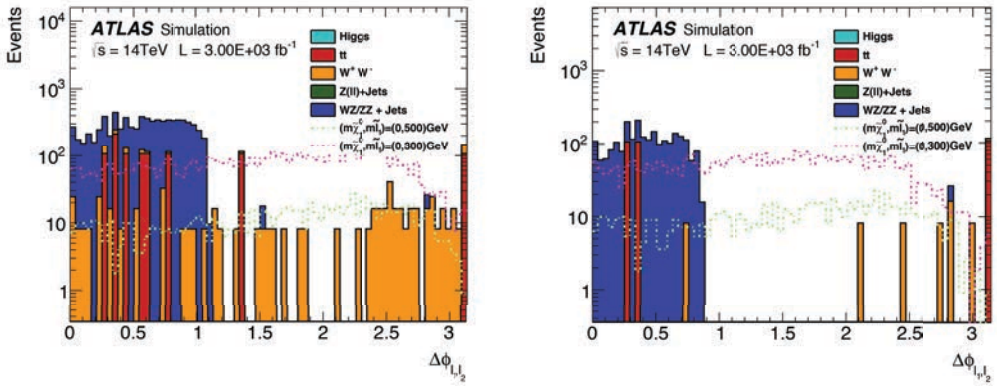

Figure 6.24: $\Delta\phi_{l_1,l_2}$ for di-slepton production with selected SM backgrounds scaled to 3000 fb^{-1} with $< \mu >= 140$, with selections $M_\Delta^R > 150$ GeV(left) and $M_\Delta^R > 200$ GeV(right).

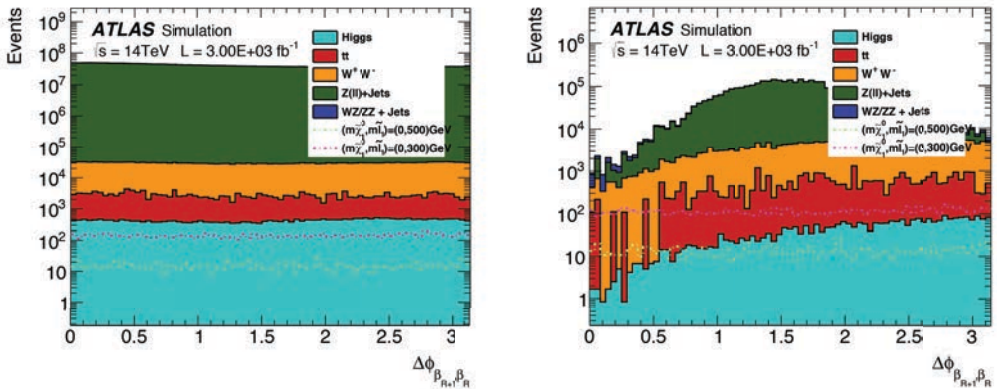

Figure 6.25: $\Delta\phi_\beta^{R+1,R}$ for di-slepton production with selected SM backgrounds scaled to 3000 fb^{-1} with $< \mu >= 140$, with no selection(left) and $M_\Delta^R > 80$ GeV(right).

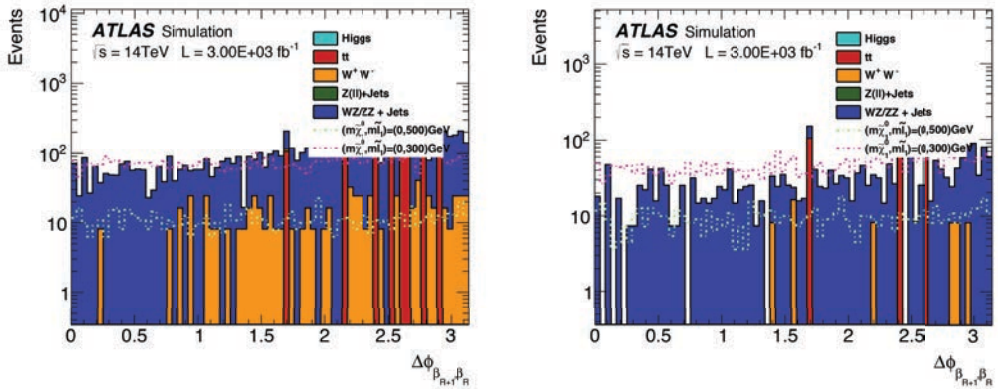

Figure 6.26: $\Delta\phi_{\beta}^{R+1,R}$ for di-slepton production with selected SM backgrounds scaled to 3000 fb^{-1} with $< \mu >= 140$, with selections $M_{\Delta}^{R} > 150$ GeV(left) and $M_{\Delta}^{R} > 200$ GeV(right).

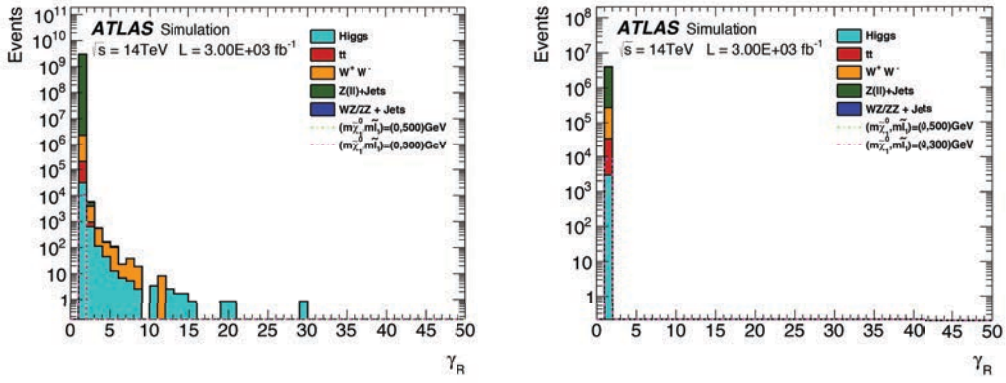

Figure 6.27: γ_R for di-slepton production with selected SM backgrounds scaled to 3000 fb^{-1} with $< \mu >= 140$, with no selection(left) and $M_{\Delta}^{R} > 80$ GeV(right).

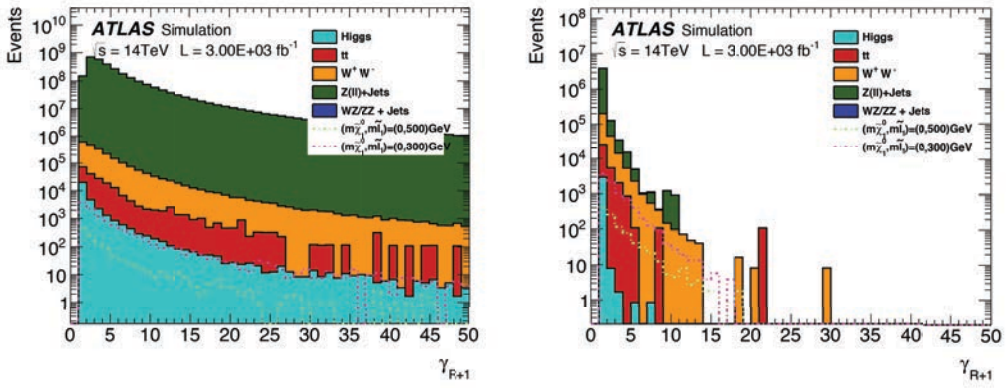

Figure 6.28: γ_{R+1} for di-slepton production with selected SM backgrounds scaled to 3000 fb^{-1} with $< \mu >= 140$, with no selection(left) and $M_{\Delta}^{R} > 80$ GeV(right).

6.3 Di-Chargino production

6.3.1 Analysis for Phase-I: 300fb^{-1} with $< \mu >= 60$

Di-chargino production processes are compared to the selected background samples, with neutralino masses set to 0 GeV and chargino masses set to 300 GeV and 500 GeV, matching the selected masses of the sleptons in the previous analysis. These signal processes have a higher cross section than the slepton production processes, however the mixed flavour lepton(and transverse momenta requirements on them) selection only yields around 20% of the signal events as opposed to the 40% of signal in the slepton analysis.

The mass variable M_{Δ}^{R} is shown in Figure 6.29. The end point seems to underestimate the mass splitting between the neutralino and the parent SUSY particle in the signal as opposed to the slepton analysis. In comparison with the slepton analysis, the Z+jets and WZ/ZZ+jets backgrounds are significantly smaller with the remaining background having a similar shape as with the same flavour lepton selection. This is due to the Z boson decay into a fermion and anti-fermion pair, which cannot have mixed flavour. As a result the selected signal samples can be separated from background through selections on M_{Δ}^{R}. We make selections at $M_{\Delta}^{R} > 80$, 150 and 200 GeV. Table 6.5 shows the number of events passing with each selection on M_{Δ}^{R}, with Table 6.6 showing the effect relative to the events passing the initial selection. With the last selection on M_{Δ}^{R}, there are around 100 to 140 signal events remaining and around 10 background events.

The other mass variable $\sqrt{\hat{s}}_{R}$, shown in Figures 6.30 and 6.31, is also underestimated significantly, this is expected when there are massive contributions to the E_{T}^{miss}, as mentioned in section 4.2. As a result, the signal seems to be shadowed by SM background, sharing a similar shape, with the exception of in the selections with $M_{\Delta}^{R} > 150$ GeV, where the number of signal events outnumber the background.

Figure 6.32 shows $\cos\theta_{R+1}$. Signal and background events favour a $\cos(\theta_{R+1})$ value of 0 with a decline in events towards 1. There is minimal correlation between high values of M_{Δ}^{R} and this variable. The effect of the selections $M_{\Delta}^{R} > 150$ GeV and $M_{\Delta}^{R} > 200$ GeV are shown in Figure 6.33. The shape of these distributions remains unchanged with a drop in magnitude.

The angle $\Delta\phi_{R}^{\beta}$ is shown in Figure 6.34 and 6.35. Both signal and background events are distributed over the entire range of $\Delta\phi_{R}^{\beta}$ from 0 to π, with a larger amount of events near π. The first selection on M_{Δ}^{R} at 80 GeV removes a large portion of background in angles less than 1.5, with the Higgs background constrained to $\Delta\phi_{R}^{\beta} > 2$. In that same region the signal with the 300 GeV slepton is of the same order as the background.

The angle $\Delta\phi_{\ell_1,\ell_2}$ similarly features a slight rise in events towards π with some subtle differences to $\Delta\phi_R^\beta$, as shown in Figure 6.36 and 6.37. The first selection on $M_\Delta^R > 80$ GeV, removes the events at larger angular values, constraining the Higgs background to values less than 1.5, and causing a dip in signal and backgrounds near π.

The angular variable $\Delta\phi_\beta^{R+1,R}$ is the difference between the azimuthal angle of the two boosts in the super razor framework. Both signal and background events do not show any interesting distributions in this variable, which are shown in the Figures 6.38 and 6.39. The selections on M_Δ^R do not create any interesting distributions in this variable.

The Lorentz factor for the first transformation is shown in Figure 6.40 and the second factor shown in Figure 6.41. The selections on M_Δ^R remove events with larger Lorentz factors, with no discrimination between signal and background.

The mixed flavour selection coupled with the selection on M_Δ^R gives a clear discrimination between the di-chargino signal and SM background. However, at Phase-I, the number of passing signal event with the more stricter selections M_Δ^R is quite low.

Table 6.5: The number of passing events from each selection. The format of the last two headings are $(m\tilde{\chi}_1^0, m\tilde{\chi}_1^\pm)$. "No selection" is the initial number of events with two leptons that are considered. The "charg selec" refers to the opposite flavour lepton and momentum requirements on the leptons as described in section 6.1. c_Mx refers to the "charg selec" in conjunction with the selection $M_\Delta^R > x$ GeV.

selection	Higgs	$t\bar{t}$	W^+W^-	$Z(ll)$+jets	WZ/ZZ +jets	(0,300) GeV	(0,500) GeV
No selection	48415 ± 61	1976.0e+04 ± 1.4e+04	958690 ± 880	5629.3e+05 ± 2.0e+05	729340 ± 960	20760 ± 110	2875 ± 15
charg selec	3070 ± 16	20220 ± 460	198400 ± 400	259.8e+03 ± 4.3e+03	5868 ± 77	4304 ± 49	525.8 ± 6.3
c_M80	90.9 ± 2.8	2920 ± 180	12200 ± 100	0 ± 0	303 ± 17	2155 ± 35	360.7 ± 5.2
c_M150	0 ± 0	63 ± 26	28.5 ± 4.8	0 ± 0	5.2 ± 2.4	581 ± 18	185.5 ± 3.7
c_M200	0 ± 0	0 ± 0	7.3 ± 2.4	0 ± 0	0.73 ± 0.73	142.7 ± 8.9	104.5 ± 2.7

Table 6.6: The percentage of events surviving relative to the initial triggered events presented in table 6.5

selection	$(m\tilde{\chi}_1^0, m\tilde{\chi}_1^{\pm}) = (0, 300)GeV$	$(m\tilde{\chi}_1^0, m\tilde{\chi}_1^{\pm}) = (0, 500)GeV$
No selection	100	100
charg selec	20.73	18.29
c_M80	10.38	12.55
c_M150	2.80	6.45
c_M200	0.69	3.63

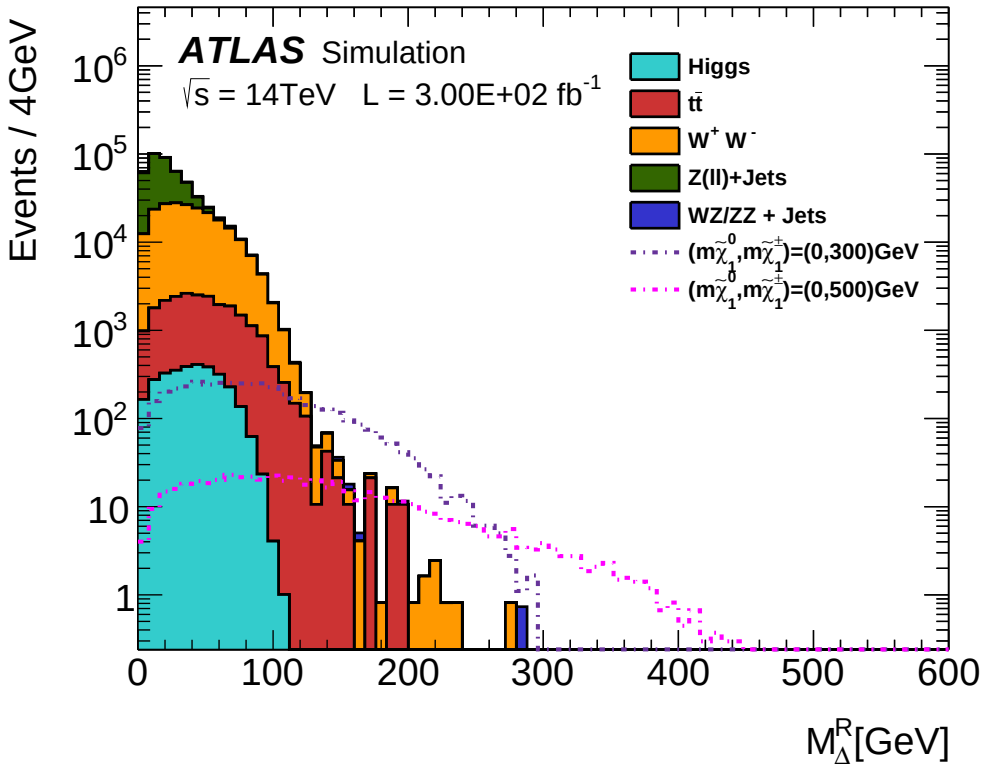

Figure 6.29: M_Δ^R for di-chargino production and selected SM backgrounds scaled to 300 fb^{-1} with $< \mu >= 60$.

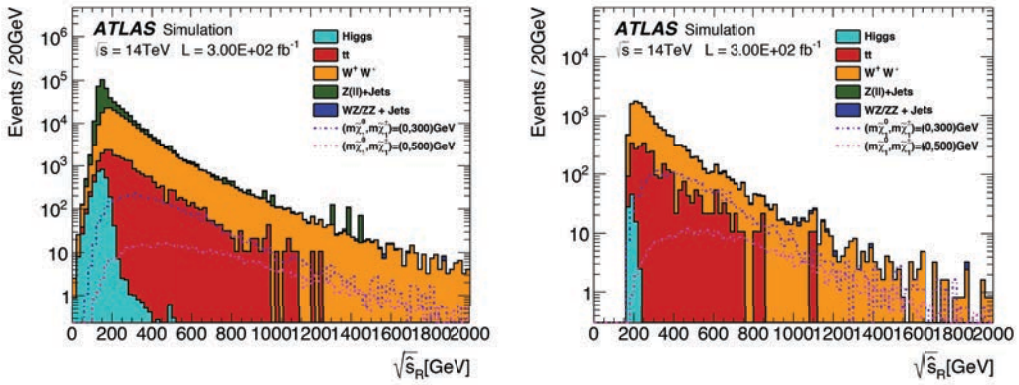

Figure 6.30: $\sqrt{\hat{s}_R}$ for di-chargino production and selected SM backgrounds scaled to 300 fb^{-1} with $< \mu >= 60$ with no selection(left) and $M_\Delta^R > 80$ GeV(right).

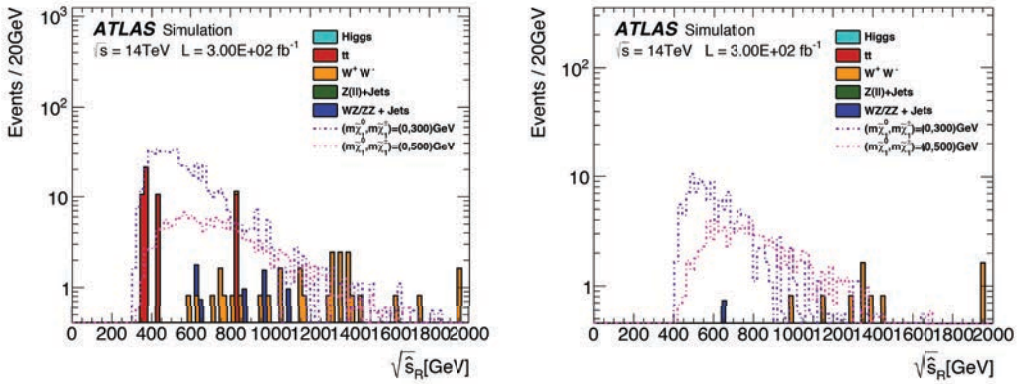

Figure 6.31: $\sqrt{\hat{s}_R}$ for di-chargino production and selected SM backgrounds scaled to 300 fb^{-1} with $< \mu >= 60$ with selections $M_\Delta^R > 150$ GeV (left) and $M_\Delta^R > 200$ GeV(right).

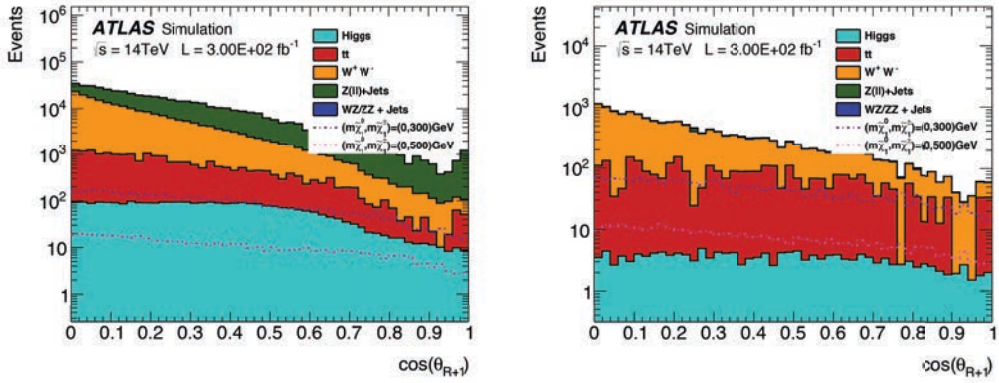

Figure 6.32: $\cos\theta_{R+1}$ for di-chargino production and selected SM backgrounds scaled to 300 fb^{-1} with $< \mu >= 60$ with selections $M_{\Delta}^{R} > 0$ GeV(left) and $M_{\Delta}^{R} > 80$ GeV(right).

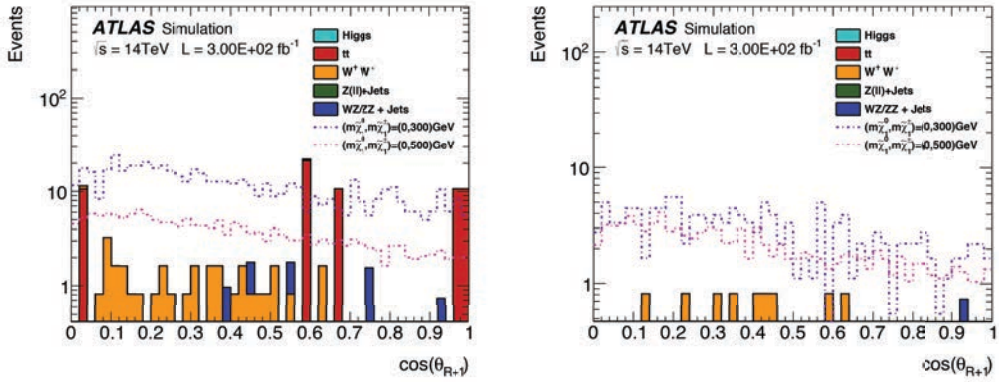

Figure 6.33: $\cos\theta_{R+1}$ for di-chargino production and selected SM backgrounds scaled to 300 fb^{-1} with $< \mu >= 60$ with selections $M_{\Delta}^{R} > 150$ GeV(left) and $M_{\Delta}^{R} > 200$ GeV(right).

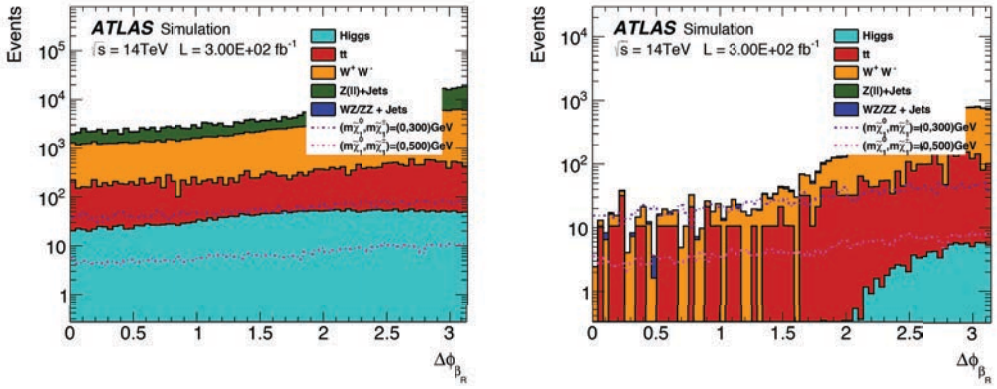

Figure 6.34: $\Delta\phi_R^\beta$ for di-chargino production and selected SM backgrounds scaled to 300 fb^{-1} with $< \mu >= 60$ with no selection(left) and $M_\Delta^R > 80$ GeV(right).

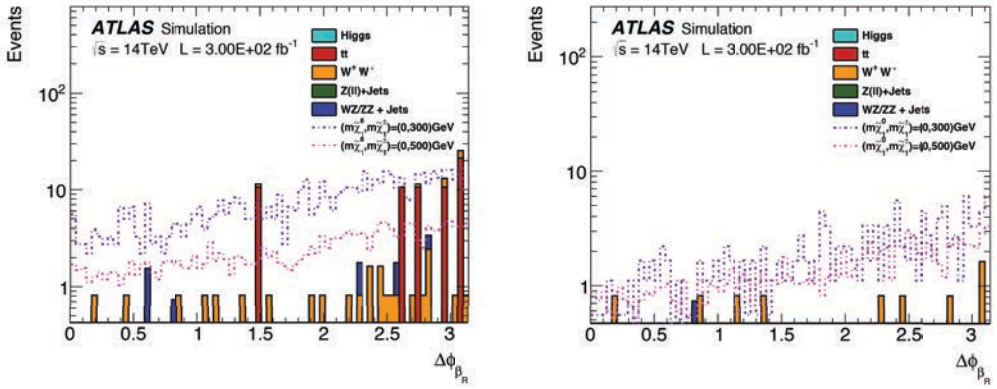

Figure 6.35: $\Delta\phi_R^\beta$ for di-chargino production and selected SM backgrounds scaled to 300 fb^{-1} with $< \mu >= 60$ with selections $M_\Delta^R > 150$ GeV(left) and $M_\Delta^R > 200$ GeV(right).

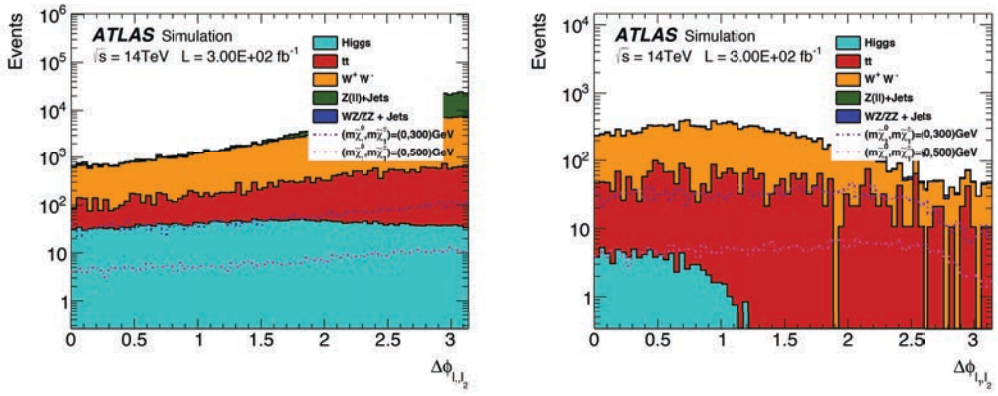

Figure 6.36: $\Delta\phi_{\ell_1,\ell_2}$ for di-chargino production and selected SM backgrounds scaled to 300 fb^{-1} with $< \mu >= 60$ with no selection(left) and $M_\Delta^R > 80$ GeV(right).

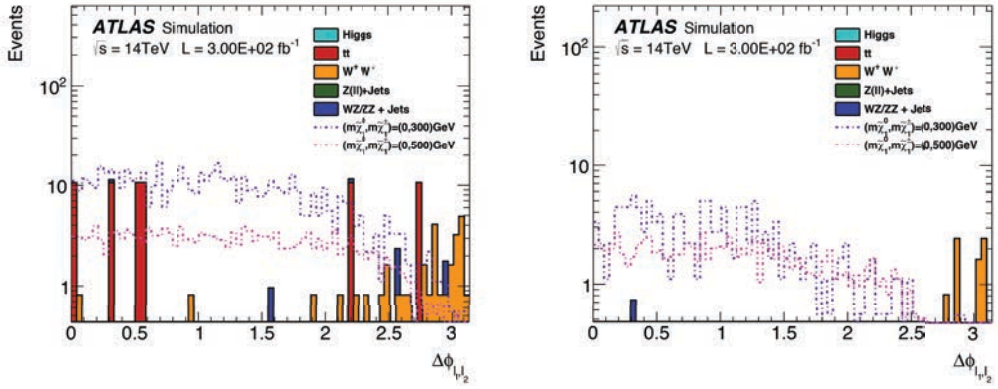

Figure 6.37: $\Delta\phi_{\ell_1,\ell_2}$ for di-chargino production and selected SM backgrounds scaled to 300 fb^{-1} with $< \mu >= 60$ with selections $M_\Delta^R > 150$ GeV(left) and $M_\Delta^R > 200$ GeV(right).

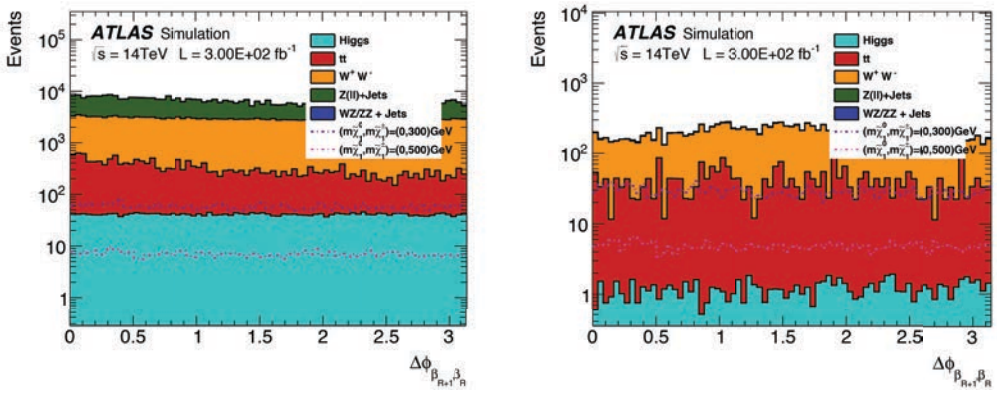

Figure 6.38: $\Delta\phi_\beta^{R+1,R}$ for di-chargino production and selected SM backgrounds scaled to 300 fb^{-1} with $< \mu >= 60$ with no selection(left) and $M_\Delta^R > 80$ GeV(right).

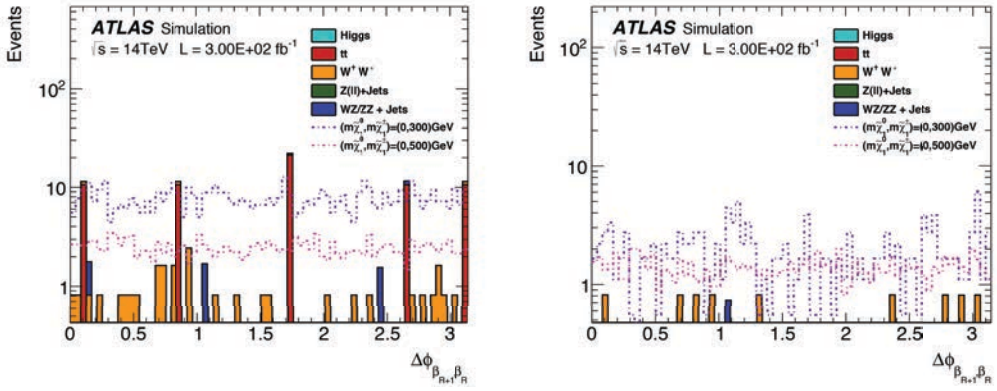

Figure 6.39: $\Delta\phi_\beta^{R+1,R}$ for di-chargino production and selected SM backgrounds scaled to 300 fb^{-1} with $< \mu >= 60$ with selections $M_\Delta^R > 150$ GeV(left) and $M_\Delta^R > 200$ GeV(right).

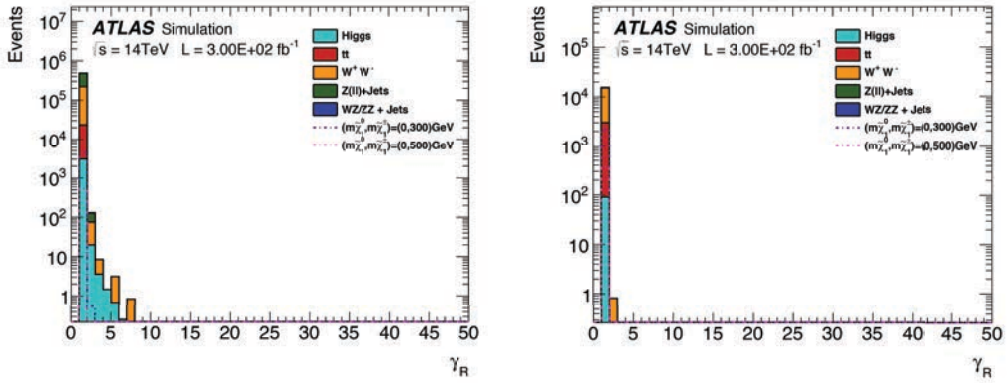

Figure 6.40: γ_R for di-chargino production and selected SM backgrounds scaled to 300 fb^{-1} with $< \mu >= 60$ with no selection(left) and $M_\Delta^R > 80$ GeV(right).

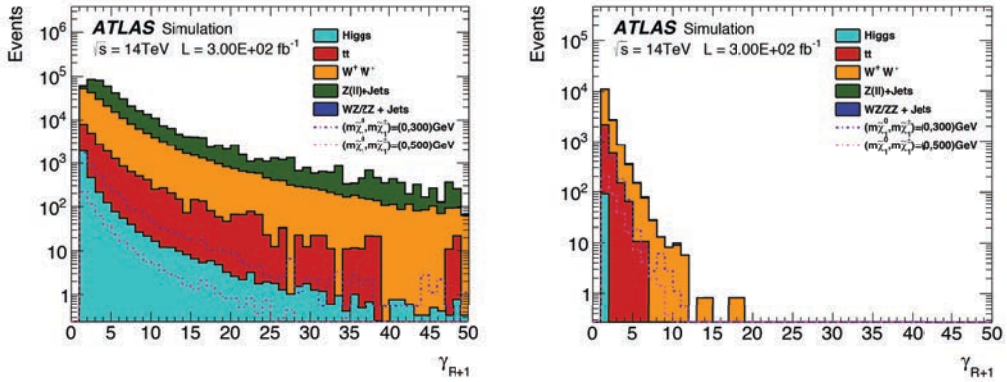

Figure 6.41: γ_{R+1} for di-chargino production and selected SM backgrounds scaled to 300 fb^{-1} with $< \mu >= 60$ with no selection(left) and $M_\Delta^R > 80$ GeV(right).

6.3.2 Analysis for Phase-II: 3000fb^{-1} with $< \mu >= 140$

Di-chargino production processes are compared to the selected background samples at Phase-II detector conditions, with neutralino masses set to 0 GeV and chargino masses set to 300 GeV and 500 GeV, matching the selected masses of the sleptons in the previous analysis.

We also compare the effect of more massive neutralinos with a 500 GeV chargino have on M_{Δ}^{R}, which is shown in Figure 6.42. The endpoint of M_{Δ}^{R} overestimates the mass splitting between the parent chargino and daughter neutralino, however it becomes closer to the mass splitting with smaller neutralino mass.

M_{Δ}^{R} with background compared to the two signal processes is shown in Figure 6.43. At higher luminosity, the end point of the distributions of M_{Δ}^{R} better approximates the mass splitting in the 500 GeV chargino mass signal.

We make three selections on M_{Δ}^{R}, at 80 GeV, 150 GeV and 200 GeV as for the slepton study. The Table 6.8 shows the events that pass each selection and table 6.9 shows the percentages relative to the initial event selection. With the last selection on M_{Δ}^{R}, there are around 1040 to 1670 signal events remaining and around 200 background events. The Table 6.7 shows the efficiency the selections on M_{Δ}^{R} have on the signal with massive neutralinos. The larger the mass difference between the chargino and neutralino, the more events pass the M_{Δ}^{R} selections, with the 400 GeV neutralino case having 0 events passing the final selection and the massless neutralino case allowing 1044 events passing the same selection.

The other mass variable $\sqrt{\hat{s}}_{R}$ is shown with no selection and the first selection on M_{Δ}^{R} in Figure 6.44. The presence of neutrinos in the decay is, as expected, skewing the peak of the signal to lower values. The tail of the signals have a higher relative amount of events compared to the background. This variable with the other selections is shown in Figure 6.45. The two signal samples maintain their shape and have very similar magnitude to each other in contrast to the slepton signals.

The angular variable $\cos\theta_{R+1}$ can be seen in Figures 6.46 and 6.47. In this variable, the signal and background events are distributed across all values, with events favouring values near 0 as opposed to 1. The selections on M_{Δ}^{R} lower the magnitude with little effect on the shape of the distribution of the signal, and also remove background events indiscriminately.

The angle $\Delta\phi_{R}^{\beta}$ features a rise in events for both background and signal for values approaching π. The first selection on M_{Δ}^{R} eliminates a significant portion of background events in the region $\Delta\phi_{R}^{\beta} < 1.5$, with the complete removal of Higgs background in that region, as seen in Figure 6.48. The remaining selections on M_{Δ}^{R} further remove background events with low values

of $\Delta\phi_R^\beta$, while allowing signal events to populate that region, as shown in Figure 6.49.

The lepton angular difference, $\Delta\phi_{\ell_1,\ell_2}$, is shown in Figures 6.50 and 6.51. The signal and background have a slight rise towards π, with the $Z(ll)$+jets background rising steeper than the other backgrounds. The first selection on M_Δ^R removes background and signal events near π, with the Higgs background featuring an endpoint to its distribution. This Higgs background endpoint is slightly larger at this luminosity than in the Phase-I analysis.

The angle $\Delta\phi_\beta^{R+1,R}$ is shown in Figures 6.52 and 6.53. The distributions do not hold any discriminatory power with selections on M_Δ^R.

The Lorentz factors for the chargino production are similar to the slepton samples in that the higher Lorentz factors are correlated with lower values of M_Δ^R. The Lorentz factor for the first transformation is shown in Figure 6.54, and for the second transformation in Figure 6.55.

Table 6.7: The amount of events that pass each selection and selection for di-chargino production with various neutralino masses, and 500 GeV chargino mass. The format of the headings are $(m\tilde{\chi}_1^0, m\tilde{\chi}_1^\pm)$. No selection are the events that were selected to have been identified with 2 leptons. The "charg selec" is the selection from the events which requires two mixed flavour leptons with a threshold on their momenta. The "c_Mx" are the selections with $M_\Delta^R > x$ GeV in addition to the selection in "charg selec".

selection	(0,500)GeV	(100,500)GeV	(200,500)GeV	(300,500)GeV	(400,500)GeV
No selection	28750 ± 150	28480 ± 140	27920 ± 140	26160 ± 140	23380 ± 120
charg selec	5258 ± 63	5142 ± 62	5089 ± 61	4756 ± 58	3841 ± 50
c_M80	3607 ± 52	3452 ± 50	3216 ± 48	2528 ± 42	992 ± 26
c_M150	1855 ± 37	1741 ± 36	1431 ± 32	778 ± 23	22.5 ± 3.9
c_M200	1044 ± 28	957 ± 27	675 ± 22	247 ± 13	0 ± 0

Table 6.8: Number of events passing each selection process. The format of the last two headings are $(m\tilde{\chi}_1^0, m\tilde{\chi}_1^{\pm})$. No selection are the events that where selected to have been identified with 2 leptons. The "charg selec" is the selection from the events which requires two mixed flavour leptons with a threshold on their momenta. The "c_Mx" are the selections with $M_\Delta^R > x$ GeV in addition to the selection in "charg selec".

selection	Higgs	$t\bar{t}$	W^+W^-	$Z(ll)$+jets	WZ/ZZ +jets	(0,300) GeV	(0,500) GeV
No selection	458260 ± 610	2388.0e+05 ± 1.6e+05	9591.5e+03 ± 8.8e+03	5620.8e+06 ± 2.0e+06	7293.4e+03 ± 9.6e+03	207.6e+03 ± 1.1e+03	28750 ± 150
charg selec	30740 ± 160	152.6e+03 ± 4.0e+03	1984.4e+03 ± 4.0e+03	263.3e+04 ± 4.4e+04	58680 ± 770	43040 ± 490	5258 ± 63
c_M80	2940 ± 50	32.0e+03 ± 1.8e+03	228.1e+03 ± 1.4e+03	8.4e+03 ± 2.2e+03	6360 ± 250	22090 ± 350	3607 ± 52
c_M150	0 ± 0	1060 ± 340	742 ± 78	0 ± 0	99 ± 32	6300 ± 190	1855 ± 37
c_M200	0 ± 0	110 ± 110	73 ± 24	0 ± 0	17 ± 12	1665 ± 96	1044 ± 28

Table 6.9: Percentage of surviving events relative to the initial selection rounded to two decimal places.

selection	$(\mathrm{m}\tilde{\chi}_1^0, \mathrm{m}\tilde{\chi}_1^{\pm}) = (0, 300) GeV$	$(\mathrm{m}\tilde{\chi}_1^0, \mathrm{m}\tilde{\chi}_1^{\pm}) = (0, 500) GeV$
No selection	100	100
charg selec	20.73	18.29
c_M80	10.64	12.55
c_M150	3.03	6.45
c_M200	0.8	3.63

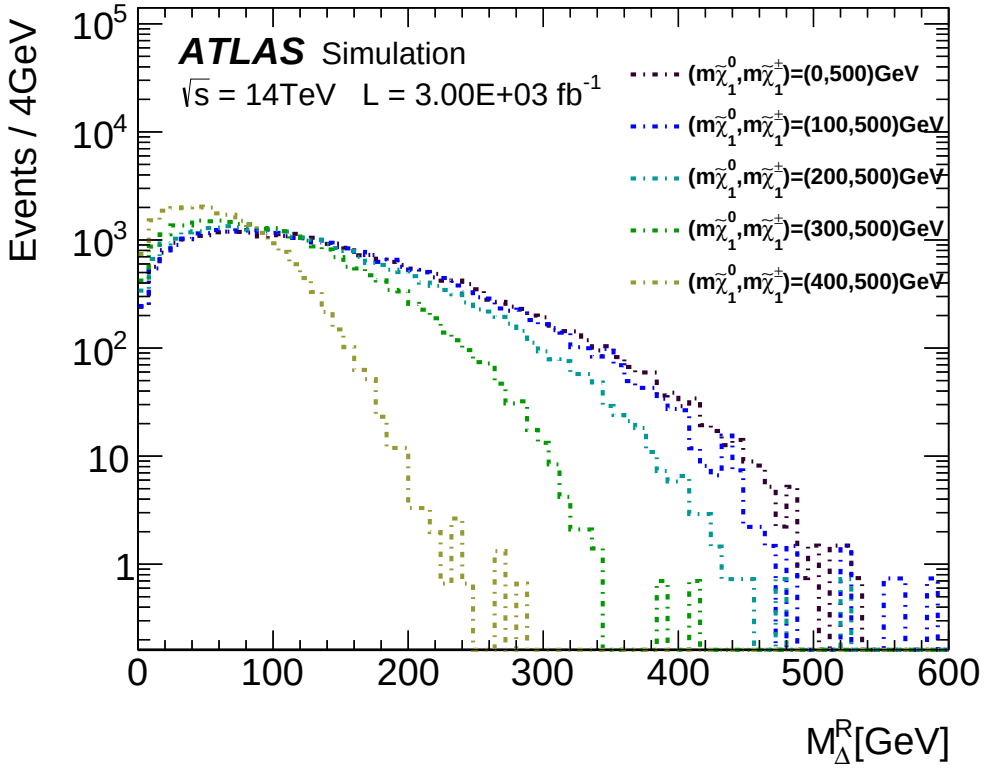

Figure 6.42: M_Δ^R for di-chargino production at various neutralino masses scaled to 3000 fb^{-1} with $< \mu >= 140$.

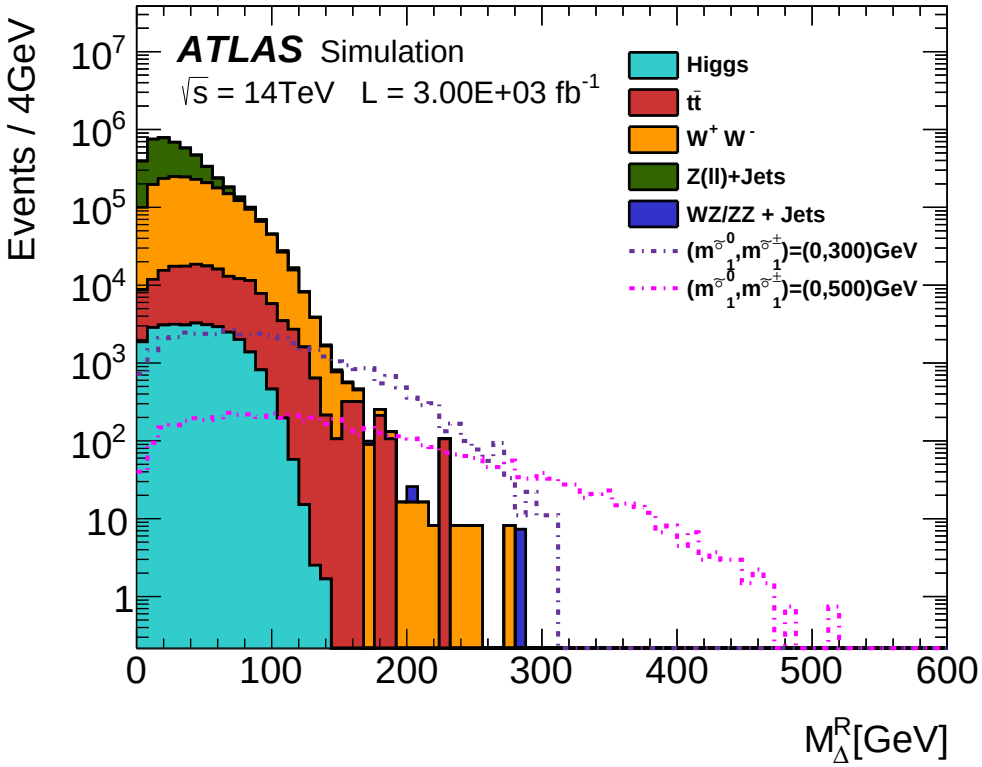

Figure 6.43: M_Δ^R for di-chargino production and selected SM backgrounds, with the mixed flavor lepton selection and scaled to 3000 fb^{-1} with $< \mu >=$ 140.

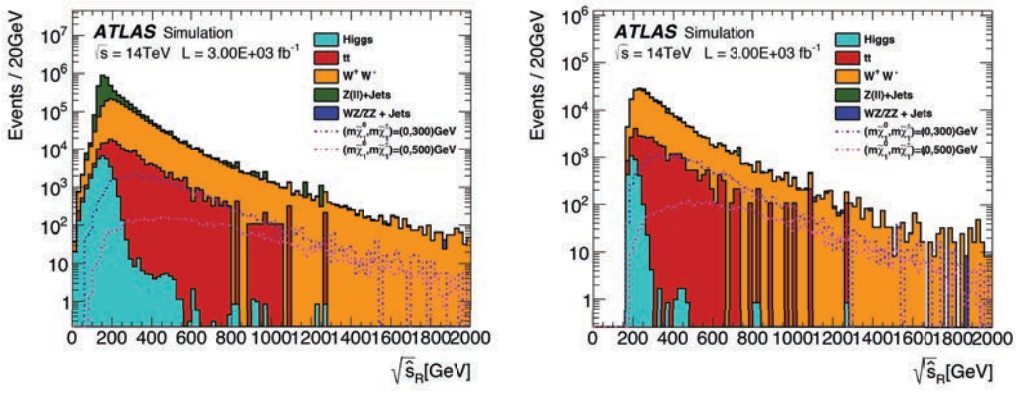

Figure 6.44: $\sqrt{\hat{s}}_R$ for di-chargino production and selected SM backgrounds scaled to 3000 fb^{-1} with $< \mu >=$ 140, with no selection(left) and $M_\Delta^R > 80$ GeV(right).

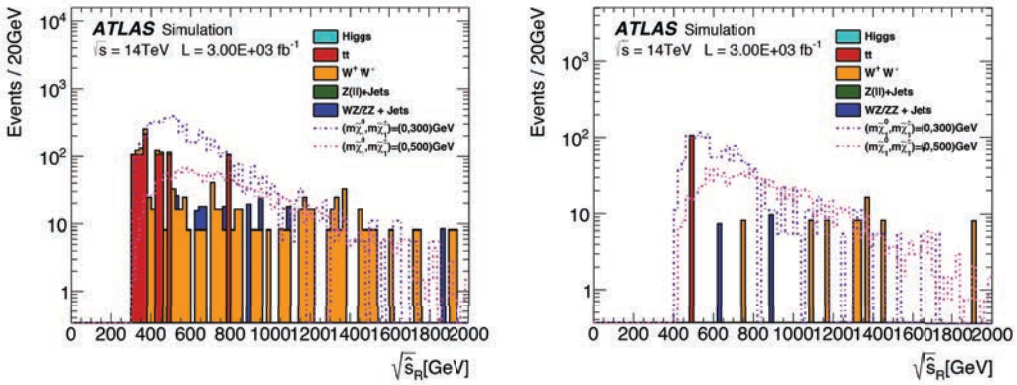

Figure 6.45: $\sqrt{\hat{s}_R}$ for di-chargino production and selected SM backgrounds scaled to 3000 fb^{-1} with $< \mu >= 140$, with selections $M_\Delta^R > 150$ GeV(left) and $M_\Delta^R > 200$ GeV(right).

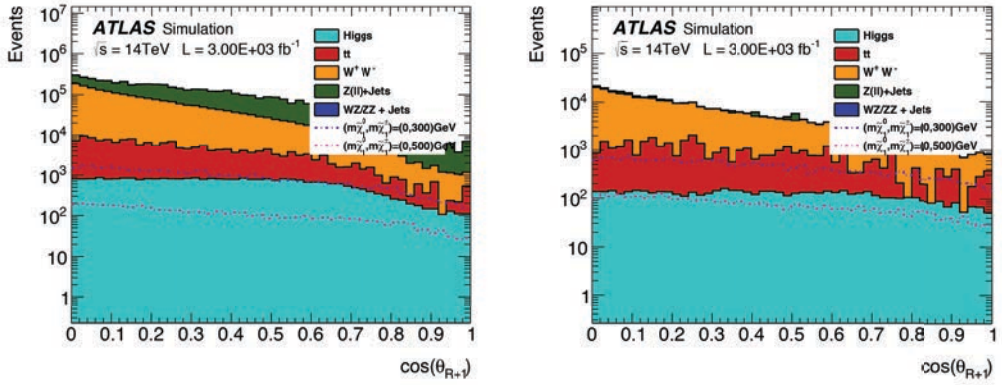

Figure 6.46: cosθ_{R+1} for di-chargino production and selected SM backgrounds scaled to 3000 fb^{-1} with $< \mu >= 140$, with no selection (left) and $M_\Delta^R > 80$ GeV (right).

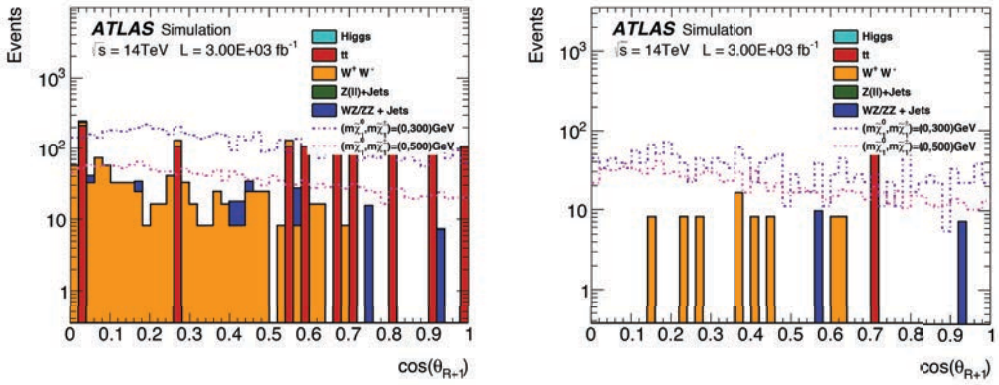

Figure 6.47: $\cos\theta_{R+1}$ for di-chargino production and selected SM backgrounds scaled to 3000 fb^{-1} with $< \mu >= 140$, with selections $M_{\Delta}^{R} > 150$ GeV (left) and $M_{\Delta}^{R} > 200$ GeV (right).

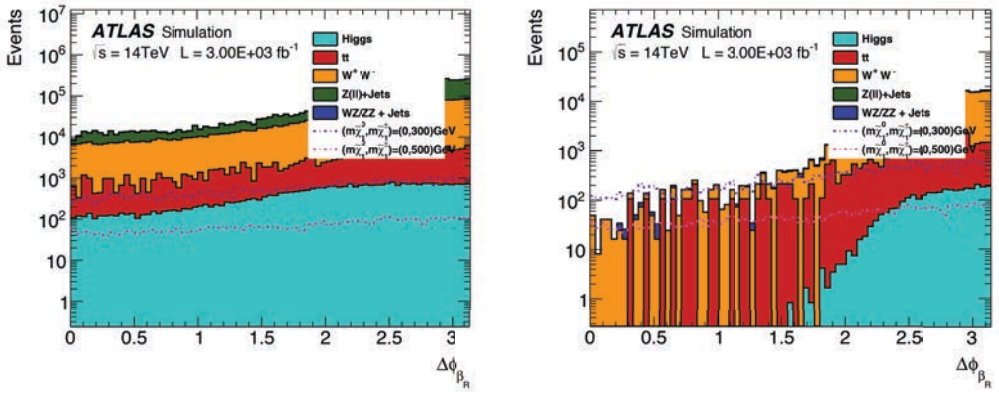

Figure 6.48: $\Delta\phi_{R}^{\beta}$ for di-chargino production and selected SM backgrounds scaled to 3000 fb^{-1} with $< \mu >= 140$, with no selection and $M_{\Delta}^{R} > 80$ GeV(right).

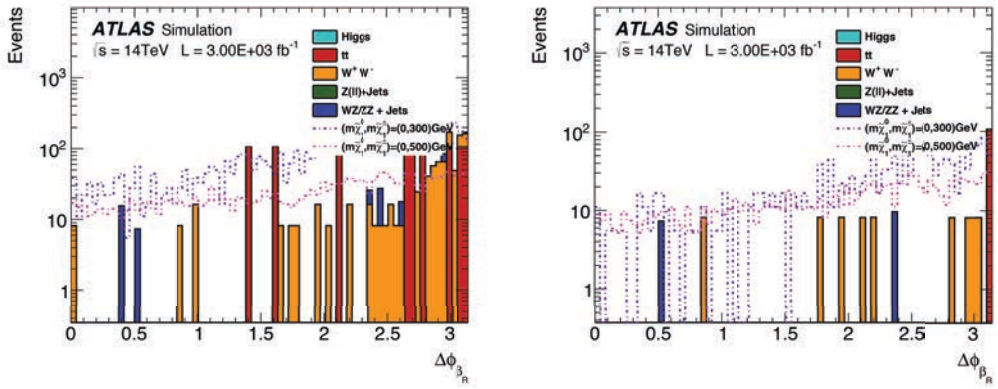

Figure 6.49: $\Delta\phi_R^\beta$ for di-chargino production and selected SM backgrounds scaled to 3000 fb^{-1} with $< \mu >= 140$, with selections $M_\Delta^R > 150$ GeV (left) and $M_\Delta^R > 200$ GeV(right).

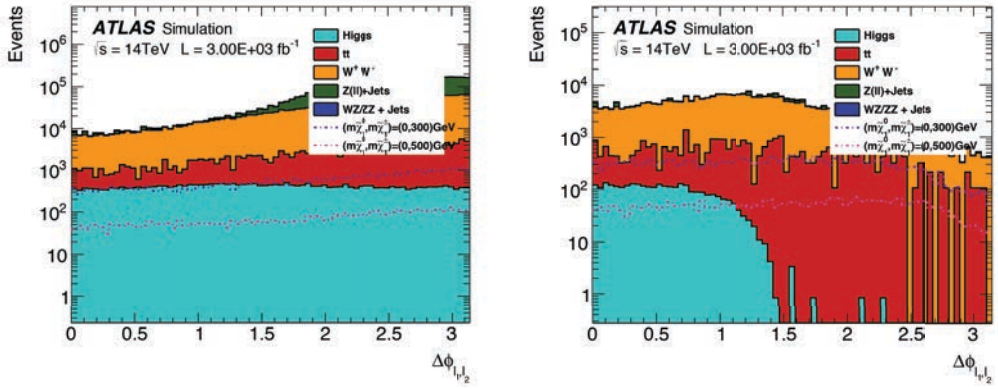

Figure 6.50: $\Delta\phi_{\ell_1,\ell_2}$ for di-chargino production and selected SM backgrounds scaled to 3000 fb^{-1} with $< \mu >= 140$, with no selection(left) and $M_\Delta^R > 80$ GeV(right).

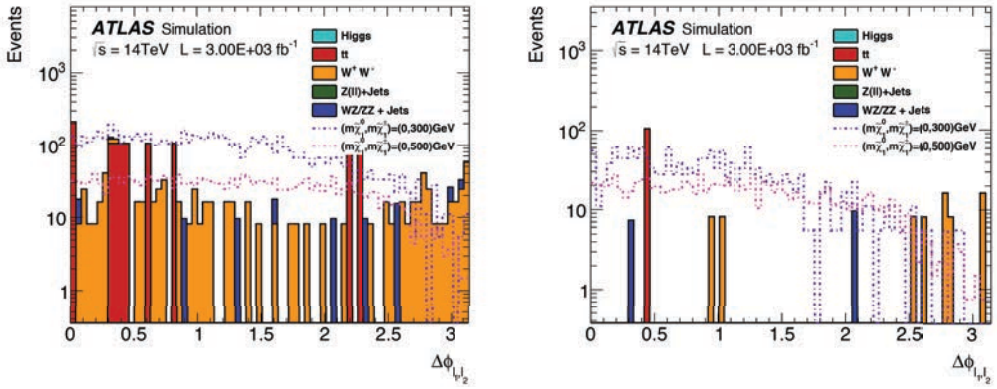

Figure 6.51: $\Delta\phi_{\ell_1,\ell_2}$ for di-chargino production and selected SM backgrounds scaled to 3000 fb^{-1} with $< \mu >= 140$, with selections $M_\Delta^R > 150$ GeV (left) and $M_\Delta^R > 200$ GeV (right).

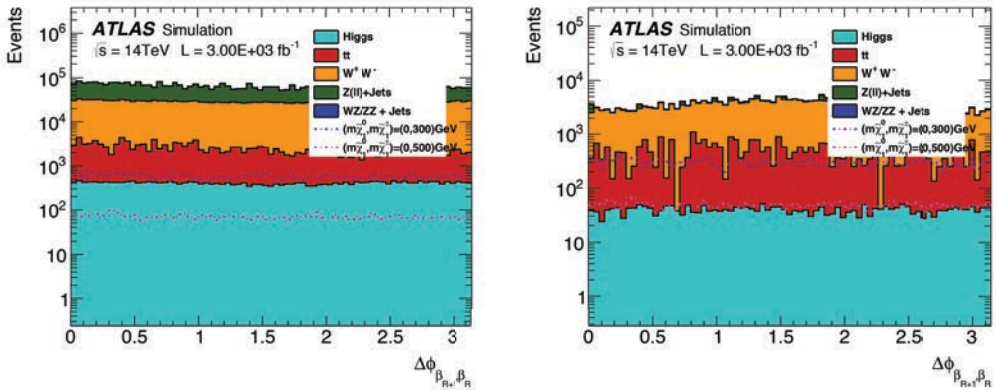

Figure 6.52: $\Delta\phi_\beta^{R+1,R}$ for di-chargino production and selected SM backgrounds scaled to 3000 fb^{-1} with $< \mu >= 140$, with no selection(left) and $M_\Delta^R > 80$ GeV(right).

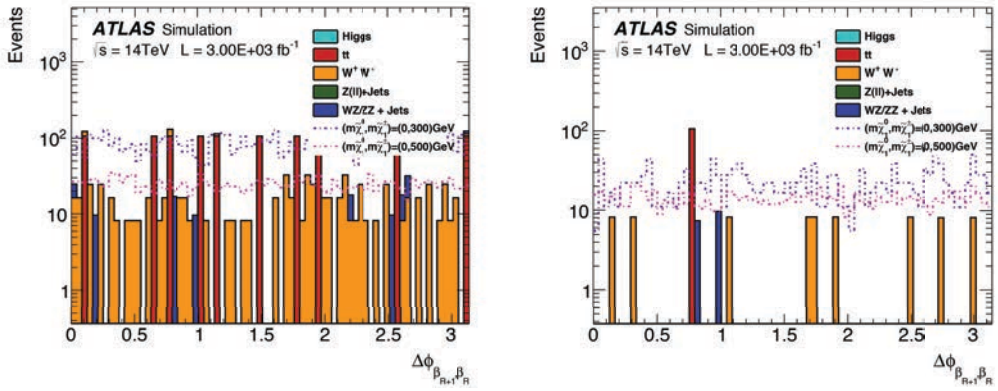

Figure 6.53: $\Delta\phi_\beta^{R+1,R}$ or di-chargino production and selected SM backgrounds scaled to 3000 fb^{-1} with $< \mu >= 140$, with selections $M_\Delta^R > 150$ GeV (left) and $M_\Delta^R > 200$ GeV (right).

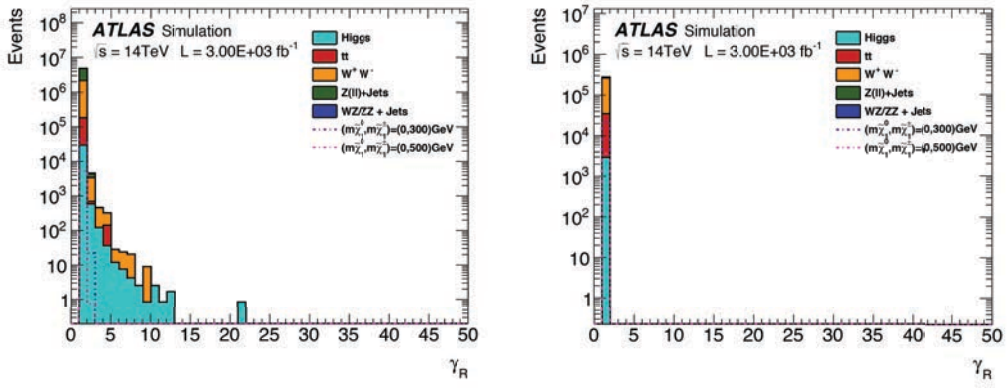

Figure 6.54: γ_R or di-chargino production and selected SM backgrounds scaled to 3000 fb^{-1} with $< \mu >= 140$, with no selection and $M_\Delta^R > 80$ GeV (right).

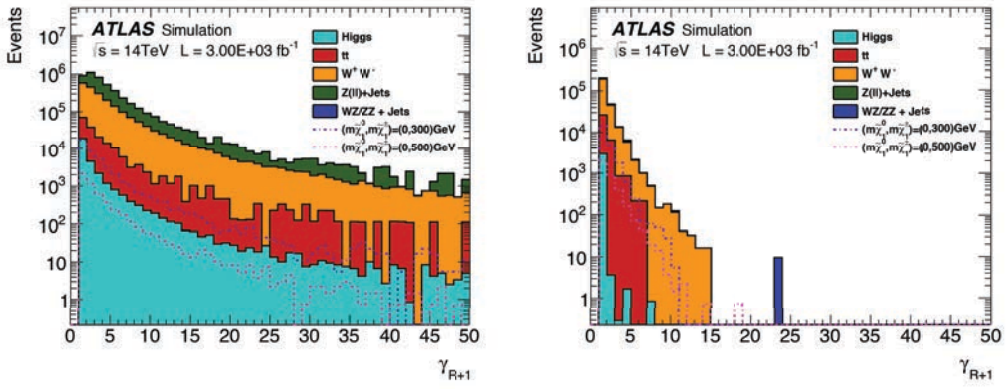

Figure 6.55: γ_{R+1} or di-chargino production and selected SM backgrounds scaled to 3000 fb^{-1} with $< \mu >= 140$, with no selection (left) and $M_{\Delta}^{R} > 80$ GeV(right).

Chapter 7

Conclusion

This thesis presents a study using Super Razor variables to address searching for $\tilde{\chi}_1^+\tilde{\chi}_1^-$ and $\tilde{l}_1^+\tilde{l}_1^-$ with the ATLAS experiment after the Phase-I and Phase-II upgrades.

The Super Razor variables arrive from a set of consecutive boosts from the lab frame to approximations of the CM frame of the decaying particles. The boost β_L takes us from the lab frame to the razor frame, and an additional boost β_R takes us to the Razor frame R. Another boost, the β_{R+1}, takes us from the Razor frame R to the Razor frames $R+1$, an approximation to the decay frames. Tightened selection criteria imposed on M_Δ^R(the super razor approximation on the mass splitting between the produced parent particle and daughter) are reliably efficient at selecting SUSY production processes over SM background. The $\sqrt{\hat{s}}_R$ variable gives the energy associated with a boost to an approximation of the pair production frame. The angle $\Delta\phi_R^\beta$ is the angle between the azimuthal angle of the sum of the visible momenta in the R frame and the boost β_R, in the Razor frame R. The variable $\cos\theta_{R+1}$ is a cosine of the angle between the boost β_{R+1} and a lepton in its Razor frame $R+1$. The angle $\Delta\phi_{l_1,l_2}$ gives the angle between the two leptons in the Razor frame R. The angle $\Delta\phi_\beta^{R+1,R}$ gives us the angle between the two boosts in the super razor framework.

In the di-slepton analysis (massless neutralino and slepton masses at 300 and 500 GeV) the selection $M_\Delta^R > 200$ GeV in conjunction with constraints on lepton momenta and flavour can yield between 70 to 350 events of signal depending on slepton mass and around 200 events of background at 300 fb^{-1}. At higher luminosity, we can obtain ten times the amount of signal events and around 2400 background events. With the selections on M_Δ^R low slepton mass the events from its production process can be seen to rise above SM backgrounds in $\sqrt{\hat{s}}_R$. In the angle $\Delta\phi_{\ell_1\ell_2}$, the signal is separated from background in the region $1 < \Delta\phi_{\ell_1\ell_2} < 2.5$ with the constraint $M_\Delta^R > 200$

GeV.

Assuming massless neutralinos, the opposite flavour selection in the di-chargino production analysis, along with the 200 GeV selection on M_{Δ}^{R} can reduce the background to a few events and the order of 100 events of di-chargino production at 300 fb^{-1}. With a sample of 3000 fb^{-1}, with the same selections we can obtain signal events in the thousands and reduce background events to about 200. When the neutralino is massive this variable becomes less effective at keeping signal events, however there are angular variables which have regions in which the signal events aren't overwhelmed by background events at lower selections on M_{Δ}^{R}. Variables such as $\Delta\phi_{R}^{\beta}$ and $\Delta\phi_{\ell_1,\ell_2}$ are promising in this case.

The limited statistics in some of the samples make definitive conclusions difficult to draw. The tighter selections on M_{Δ}^{R} leave a limited yield of events for the $t\bar{t}$ and $W^{+}W^{-}$ backgrounds, when scaled to represent the luminosities the shapes of the distributions can be difficult to see. The end point of distributions of $t\bar{t}$ background in the $\sqrt{\hat{s}}_{R}$ is also unclear. These problems would be alleviated with increased monte carlo generated data samples of these backgrounds.

Our results show that di-chargino and di-slepton production can be readily observed with the ATLAS experiment. Depending on the masses nature chooses for these objects, application of the Super-Razor variable basis will realise a discovery after phase-I or phase-II of the ATLAS upgrade program.

Appendix A

Cross sections and Filter efficiencies

The cross sections for the various samples were obtained from multiple sources, and are shown in the table below under the heading 'σ'. The cross sections of the Higgs were obtained from the Handbook of LHC Higgs Cross Sections published in a CERN report[61]. The ttbar sample cross section was obtained from the program HATHOR(HAdronic Top and Heavy quarks crOss section calculatoR) version 1.3[62]. The WW,WZ,ZZ cross sections were obtained with MCFM program with MSTW2008NLO PDF set [63]. AMI(Atlas Metadata Interface) was used to obtain the cross section of Z+Jets, and the Di-slepton production process. AMI was also used to obtain the filter efficiencies of all the datasets, which is shown in the table below under the heading 'Eff'. The Chargino production process cross section was calculated using Prospino2.1[64].

Dataset number	ptag	physicsShort	Num Events	Eff	σ(pb)
Background samples					
161005	p1087	PowhegPythia8_AU2CT10_ggH125_WW2lep_EF_15_5	2000000	4.9253E-01	1.137642
161055	p1087	PowhegPythia8_AU2CT10_VBFH125_WW2lep_EF_15_5	1000000	5.1068E-01	0.095393
105200	p1087	McAtNloJimmy_CT10_ttbar_LeptonFilter	14990000	5.4272E-01	977.7
105921	p1087	McAtNloJimmy_AUET2CT10_WpWmenuenu	495000	1.0000E+00	1.3414
105922	p1087	McAtNloJimmy_AUET2CT10_WpWmenumunu	495000	1.0000E+00	1.3435
105923	p1087	McAtNloJimmy_AUET2CT10_WpWmenutaunu	495000	1.0000E+00	1.3470
105924	p1087	McAtNloJimmy_AUET2CT10_WpWmmunuenu	495000	1.0000E+00	1.3459
105925	p1087	McAtNloJimmy_AUET2CT10_WpWmmunumunu	495000	1.0000E+00	1.3455
105926	p1087	McAtNloJimmy_AUET2CT10_WpWmmunutaunu	495000	1.0000E+00	1.3456
105927	p1087	McAtNloJimmy_AUET2CT10_WpWmtaunuenu	495000	1.0000E+00	1.3450
105928	p1087	McAtNloJimmy_AUET2CT10_WpWmtaunumunu	495000	1.0000E+00	1.3457
105929	p1087	McAtNloJimmy_AUET2CT10_WpWmtaunutaunu	485000	1.0000E+00	1.3487
147073	p1087	AlpgenJimmy_Auto_AUET2CTEQ6L1_ZeeNp0	4880000	1.0000E+00	1306.4
147074	p1087	AlpgenJimmy_Auto_AUET2CTEQ6L1_ZeeNp1	1900000	1.0000E+00	334.37
147075	p1087	AlpgenJimmy_Auto_AUET2CTEQ6L1_ZeeNp2	710000	1.0000E+00	121.29
147076	p1087	AlpgenJimmy_Auto_AUET2CTEQ6L1_ZeeNp3	300000	1.0000E+00	40.95
147077	p1087	AlpgenJimmy_Auto_AUET2CTEQ6L1_ZeeNp4	118000	1.0000E+00	13.043
147078	p1087	AlpgenJimmy_Auto_AUET2CTEQ6L1_ZeeNp5	36700	1.0000E+00	5.0333
147081	p1087	AlpgenJimmy_Auto_AUET2CTEQ6L1_ZmumuNp0	4895000	1.0000E+00	1306.8
147082	p1087	AlpgenJimmy_Auto_AUET2CTEQ6L1_ZmumuNp1	1910000	1.0000E+00	334.55
147083	p1087	AlpgenJimmy_Auto_AUET2CTEQ6L1_ZmumuNp2	745000	1.0000E+00	121.26
147084	p1087	AlpgenJimmy_Auto_AUET2CTEQ6L1_ZmumuNp3	300000	1.0000E+00	40.905
147085	p1087	AlpgenJimmy_Auto_AUET2CTEQ6L1_ZmumuNp4	117000	1.0000E+00	13.041

147086	p1087	AlpgenJimmy_Auto_AUET2CTEQ6L1_ZmumuNp5	36900	1.0000E+00	5.0234
147089	p1087	AlpgenJimmy_Auto_AUET2CTEQ6L1_ZtautauNp0	4900000	1.0000E+00	1306.3
147090	p1087	AlpgenJimmy_Auto_AUET2CTEQ6L1_ZtautauNp1	1820000	1.0000E+00	334.47
147091	p1087	AlpgenJimmy_Auto_AUET2CTEQ6L1_ZtautauNp2	745000	1.0000E+00	121.09
147092	p1087	AlpgenJimmy_Auto_AUET2CTEQ6L1_ZtautauNp3	300000	1.0000E+00	40.866
147093	p1087	AlpgenJimmy_Auto_AUET2CTEQ6L1_ZtautauNp4	115000	1.0000E+00	13.031
147094	p1087	AlpgenJimmy_Auto_AUET2CTEQ6L1_ZtautauNp5	36800	1.0000E+00	5.0564
107104	p1581	AlpgenJimmy_AUET2CTEQ6L1_WZincllNp0	500000	1.0000E+00	1.6041
107105	p1581	AlpgenJimmy_AUET2CTEQ6L1_WZincllNp1	250000	1.0000E+00	1.2949
107106	p1581	AlpgenJimmy_AUET2CTEQ6L1_WZincllNp2	150000	1.0000E+00	8.7376E-01
107107	p1581	AlpgenJimmy_AUET2CTEQ6L1_WZincllNp3	100000	1.0000E+00	6.8769E-01
107108	p1581	AlpgenJimmy_AUET2CTEQ6L1_ZZincllNp0	500000	1.0000E+00	1.2236E
107109	p1581	AlpgenJimmy_AUET2CTEQ6L1_ZZincllNp1	250000	1.0000E+00	7.0031E-01
107110	p1581	AlpgenJimmy_AUET2CTEQ6L1_ZZincllNp2	150000	1.0000E+00	3.4545E-01
107111	p1581	AlpgenJimmy_AUET2CTEQ6L1_ZZincllNp3	100000	1.0000E+00	2.1078E-01
Di-chargino signal samples					
202515	p1087	Herwigpp_UEEE3_CTEQ6L1_C1C1_WW_mN1_0_mC1_100	50000	3.2845E-01	12.1822394250
202516	p1087	Herwigpp_UEEE3_CTEQ6L1_C1C1_WW_mN1_20_mC1_100	50000	2.4409E-01	12.1822394250
202517	p1087	Herwigpp_UEEE3_CTEQ6L1_C1C1_WW_mN1_40_mC1_100	50000	1.9904E-01	12.1822394250
202518	p1087	Herwigpp_UEEE3_CTEQ6L1_C1C1_WW_mN1_60_mC1_100	50000	1.2034E-01	12.1822394250
202519	p1087	Herwigpp_UEEE3_CTEQ6L1_C1C1_WW_mN1_0_mC1_125	50000	3.4662E-01	5.4331315462
202520	p1087	Herwigpp_UEEE3_CTEQ6L1_C1C1_WW_mN1_20_mC1_125	50000	3.4514E-01	5.4331315462
202521	p1087	Herwigpp_UEEE3_CTEQ6L1_C1C1_WW_mN1_40_mC1_125	50000	2.0183E-01	5.4331315462
202521	p1087	Herwigpp_UEEE3_CTEQ6L1_C1C1_WW_mN1_40_mC1_125	50000	2.8213E-01	5.4331315462
202522	p1087	Herwigpp_UEEE3_CTEQ6L1_C1C1_WW_mN1_60_mC1_125	50000	1.2077E-01	5.4331315462
202522	p1087	Herwigpp_UEEE3_CTEQ6L1_C1C1_WW_mN1_60_mC1_125	50000	2.3738E-01	5.4331315462
202523	p1087	Herwigpp_UEEE3_CTEQ6L1_C1C1_WW_mN1_80_mC1_125	50000	2.7653E-02	5.4331315462
202523	p1087	Herwigpp_UEEE3_CTEQ6L1_C1C1_WW_mN1_80_mC1_125	50000	1.5831E-01	5.4331315462
202524	p1087	Herwigpp_UEEE3_CTEQ6L1_C1C1_WW_mN1_0_mC1_150	50000	3.2723E-01	2.8271517195
202524	p1087	Herwigpp_UEEE3_CTEQ6L1_C1C1_WW_mN1_0_mC1_150	50000	3.6125E-01	2.8271517195
202525	p1087	Herwigpp_UEEE3_CTEQ6L1_C1C1_WW_mN1_20_mC1_150	50000	2.4594E-01	2.8271517195
202525	p1087	Herwigpp_UEEE3_CTEQ6L1_C1C1_WW_mN1_20_mC1_150	50000	3.6173E-01	2.8271517195
202526	p1087	Herwigpp_UEEE3_CTEQ6L1_C1C1_WW_mN1_40_mC1_150	50000	2.0039E-01	2.8271517195
202526	p1087	Herwigpp_UEEE3_CTEQ6L1_C1C1_WW_mN1_40_mC1_150	50000	3.5971E-01	2.8271517195
202527	p1087	Herwigpp_UEEE3_CTEQ6L1_C1C1_WW_mN1_60_mC1_150	50000	1.2077E-01	2.8271517195
202527	p1087	Herwigpp_UEEE3_CTEQ6L1_C1C1_WW_mN1_60_mC1_150	50000	3.1382E-01	2.8271517195
202528	p1087	Herwigpp_UEEE3_CTEQ6L1_C1C1_WW_mN1_80_mC1_150	50000	2.7653E-02	2.8271517195
202528	p1087	Herwigpp_UEEE3_CTEQ6L1_C1C1_WW_mN1_80_mC1_150	50000	2.6698E-01	2.8271517195
202529	p1087	Herwigpp_UEEE3_CTEQ6L1_C1C1_WW_mN1_100_mC1_150	50000	1.9165E-01	2.8271517195
202530	p1087	Herwigpp_UEEE3_CTEQ6L1_C1C1_WW_mN1_0_mC1_200	50000	3.8900E-01	0.9999487724
202531	p1087	Herwigpp_UEEE3_CTEQ6L1_C1C1_WW_mN1_20_mC1_200	50000	3.8771E-01	0.9999487724
202532	p1087	Herwigpp_UEEE3_CTEQ6L1_C1C1_WW_mN1_40_mC1_200	50000	3.8774E-01	0.9999487724
202533	p1087	Herwigpp_UEEE3_CTEQ6L1_C1C1_WW_mN1_60_mC1_200	50000	3.8733E-01	0.9999487724
202534	p1087	Herwigpp_UEEE3_CTEQ6L1_C1C1_WW_mN1_80_mC1_200	50000	3.8564E-01	0.9999487724
202535	p1087	Herwigpp_UEEE3_CTEQ6L1_C1C1_WW_mN1_100_mC1_200	50000	3.8015E-01	0.9999487724
202536	p1087	Herwigpp_UEEE3_CTEQ6L1_C1C1_WW_mN1_120_mC1_200	50000	3.1697E-01	0.9999487724
202537	p1087	Herwigpp_UEEE3_CTEQ6L1_C1C1_WW_mN1_140_mC1_200	50000	2.5248E-01	0.9999487724
202538	p1087	Herwigpp_UEEE3_CTEQ6L1_C1C1_WW_mN1_160_mC1_200	50000	1.5016E-01	0.9999487724
202539	p1087	Herwigpp_UEEE3_CTEQ6L1_C1C1_WW_mN1_0_mC1_250	50000	4.0603E-01	0.4371315218
202540	p1087	Herwigpp_UEEE3_CTEQ6L1_C1C1_WW_mN1_20_mC1_250	50000	4.0755E-01	0.4371315218
202541	p1087	Herwigpp_UEEE3_CTEQ6L1_C1C1_WW_mN1_40_mC1_250	50000	4.0750E-01	0.4371315218
202542	p1087	Herwigpp_UEEE3_CTEQ6L1_C1C1_WW_mN1_60_mC1_250	50000	4.0620E-01	0.4371315218
202543	p1087	Herwigpp_UEEE3_CTEQ6L1_C1C1_WW_mN1_80_mC1_250	50000	4.0358E-01	0.4371315218
202544	p1087	Herwigpp_UEEE3_CTEQ6L1_C1C1_WW_mN1_100_mC1_250	50000	4.0108E-01	0.4371315218
202545	p1087	Herwigpp_UEEE3_CTEQ6L1_C1C1_WW_mN1_120_mC1_250	50000	4.0070E-01	0.4371315218
202546	p1087	Herwigpp_UEEE3_CTEQ6L1_C1C1_WW_mN1_140_mC1_250	50000	3.9445E-01	0.4371315218
202547	p1087	Herwigpp_UEEE3_CTEQ6L1_C1C1_WW_mN1_160_mC1_250	50000	3.5339E-01	0.4371315218
202548	p1087	Herwigpp_UEEE3_CTEQ6L1_C1C1_WW_mN1_180_mC1_250	50000	3.0289E-01	0.4371315218
202549	p1087	Herwigpp_UEEE3_CTEQ6L1_C1C1_WW_mN1_200_mC1_250	50000	2.1522E-01	0.4371315218
202550	p1087	Herwigpp_UEEE3_CTEQ6L1_C1C1_WW_mN1_0_mC1_300	50000	4.2528E-01	0.2168252150
202551	p1087	Herwigpp_UEEE3_CTEQ6L1_C1C1_WW_mN1_50_mC1_300	50000	4.2420E-01	0.2168252150
202552	p1087	Herwigpp_UEEE3_CTEQ6L1_C1C1_WW_mN1_100_mC1_300	50000	4.1831E-01	0.2168252150
202553	p1087	Herwigpp_UEEE3_CTEQ6L1_C1C1_WW_mN1_150_mC1_300	50000	4.1368E-01	0.2168252150
202554	p1087	Herwigpp_UEEE3_CTEQ6L1_C1C1_WW_mN1_200_mC1_300	50000	4.0717E-01	0.2168252150
202555	p1087	Herwigpp_UEEE3_CTEQ6L1_C1C1_WW_mN1_250_mC1_300	50000	2.2217E-01	0.2168252150
202556	p1087	Herwigpp_UEEE3_CTEQ6L1_C1C1_WW_mN1_0_mC1_400	50000	4.5150E-01	0.0689731499
202557	p1087	Herwigpp_UEEE3_CTEQ6L1_C1C1_WW_mN1_50_mC1_400	50000	4.5082E-01	0.0689731499
202558	p1087	Herwigpp_UEEE3_CTEQ6L1_C1C1_WW_mN1_100_mC1_400	50000	4.4807E-01	0.0689731499
202559	p1087	Herwigpp_UEEE3_CTEQ6L1_C1C1_WW_mN1_150_mC1_400	50000	4.4210E-01	0.0689731499
202560	p1087	Herwigpp_UEEE3_CTEQ6L1_C1C1_WW_mN1_200_mC1_400	50000	4.3759E-01	0.0689731499
202561	p1087	Herwigpp_UEEE3_CTEQ6L1_C1C1_WW_mN1_250_mC1_400	50000	4.2545E-01	0.0689731499
202562	p1087	Herwigpp_UEEE3_CTEQ6L1_C1C1_WW_mN1_300_mC1_400	50000	4.1577E-01	0.0689731499
202563	p1087	Herwigpp_UEEE3_CTEQ6L1_C1C1_WW_mN1_350_mC1_400	50000	2.2748E-01	0.0689731499
202564	p1087	Herwigpp_UEEE3_CTEQ6L1_C1C1_WW_mN1_0_mC1_500	50000	4.7290E-01	0.0261882751
202565	p1087	Herwigpp_UEEE3_CTEQ6L1_C1C1_WW_mN1_50_mC1_500	50000	4.6801E-01	0.0261882751
202566	p1087	Herwigpp_UEEE3_CTEQ6L1_C1C1_WW_mN1_100_mC1_500	50000	4.6971E-01	0.0261882751
202567	p1087	Herwigpp_UEEE3_CTEQ6L1_C1C1_WW_mN1_150_mC1_500	50000	4.6450E-01	0.0261882751
202568	p1087	Herwigpp_UEEE3_CTEQ6L1_C1C1_WW_mN1_200_mC1_500	50000	4.6318E-01	0.0261882751
202569	p1087	Herwigpp_UEEE3_CTEQ6L1_C1C1_WW_mN1_250_mC1_500	50000	4.5495E-01	0.0261882751
202570	p1087	Herwigpp_UEEE3_CTEQ6L1_C1C1_WW_mN1_300_mC1_500	50000	4.4462E-01	0.0261882751
202571	p1087	Herwigpp_UEEE3_CTEQ6L1_C1C1_WW_mN1_350_mC1_500	50000	4.3573E-01	0.0261882751
202572	p1087	Herwigpp_UEEE3_CTEQ6L1_C1C1_WW_mN1_400_mC1_500	50000	4.2080E-01	0.0261882751
202573	p1087	Herwigpp_UEEE3_CTEQ6L1_C1C1_WW_mN1_450_mC1_500	50000	2.2842E-01	0.0261882751

Di-slepton signal samples					
164449	p1087	Herwigpp_pMSSM_DLiSlep_MSL_500_M1_000	20000	1.0000E+00	6.0000E-03
175578	p1087	Herwigpp_pMSSM_DLiSlep_MSL_300_M1_000	20000	1.0000E+00	1.2750E-02

Bibliography

[1] J. J. Thomson. Xl. cathode rays. *Philosophical Magazine Series 5*, 44(269):293–316, 1897.

[2] Steven Weinberg. A model of leptons. *Phys. Rev. Lett.*, 19:1264–1266, Nov 1967.

[3] S.L. Glashow. Partial Symmetries of Weak Interactions. *Nucl.Phys.*, 22:579–588, 1961.

[4] Steven Weinberg. Baryon- and lepton-nonconserving processes. *Phys. Rev. Lett.*, 43:1566–1570, Nov 1979.

[5] The ATLAS Collaboration. Observation of a new particle in the search for the standard model higgs boson with the {ATLAS} detector at the {LHC}. *Physics Letters B*, 716(1):1 – 29, 2012.

[6] F. Englert and R. Brout. Broken symmetry and the mass of gauge vector mesons. *Phys. Rev. Lett.*, 13:321–323, Aug 1964.

[7] Peter W. Higgs. Broken symmetries and the masses of gauge bosons. *Phys. Rev. Lett.*, 13:508–509, Oct 1964.

[8] Hironari Miyazawa. Baryon number changing currents. *Progress of Theoretical Physics*, 36(6):1266–1276, 1966.

[9] P. Ramond. Dual theory for free fermions. *Phys. Rev. D*, 3:2415–2418, May 1971.

[10] Yu.A. Golfand and E.P. Likhtman. Extension of the Algebra of Poincare Group Generators and Violation of p Invariance. *JETP Lett.*, 13:323–326, 1971.

[11] A. Neveu and J.H. Schwarz. Factorizable dual model of pions. *Nucl.Phys.*, B31:86–112, 1971.

[12] A. Neveu and J.H. Schwarz. Quark Model of Dual Pions. *Phys.Rev.*, D4:1109–1111, 1971.

[13] Jean-Loup Gervais and B. Sakita. Field Theory Interpretation of Supergauges in Dual Models. *Nucl.Phys.*, B34:632–639, 1971.

[14] D.V. Volkov and V.P. Akulov. Is the Neutrino a Goldstone Particle? *Phys.Lett.*, B46:109–110, 1973.

[15] J. Wess and B. Zumino. A Lagrangian Model Invariant Under Supergauge Transformations. *Phys.Lett.*, B49:52, 1974.

[16] J. Wess and B. Zumino. Supergauge Transformations in Four-Dimensions. *Nucl.Phys.*, B70:39–50, 1974.

[17] The ATLAS Collaboration. The ATLAS Experiment at the CERN Large Hadron Collider. *Journal of Instrumentation*, 3(08):S08003, 2008.

[18] P. A. M. Dirac. The Quantum Theory of the Electron. *Royal Society of London Proceedings Series A*, 117:610–624, February 1928.

[19] PBS NOVA, Fermilab, Office of Science, United States Department of Energy, Particle Data Group, 2014.

[20] R. Penco and D. Mauro. Perturbation theory via Feynman diagrams in classical mechanics. *Eur.J.Phys.*, 27:1241–1250, 2006.

[21] Stephen P. Martin. A Supersymmetry primer. *Adv.Ser.Direct.High Energy Phys.*, 21:1–153, 2010.

[22] Katherine Garrett and Gintaras Duda. Dark Matter: A Primer. *Adv.Astron.*, 2011:968283, 2011.

[23] Fred Jegerlehner and Andreas Nyffeler. The muon . *Physics Reports*, 477(1–3):1 – 110, 2009.

[24] James P. Miller, Eduardo de Rafael, and B. Lee Roberts. Muon (g-2): Experiment and theory. *Rept. Prog. Phys.*, 70:795, 2007.

[25] Matthew R. Buckley, Dan Hooper, and Jason Kumar. Phenomenology of dirac neutralino dark matter. *Phys. Rev. D*, 88:063532, Sep 2013.

[26] Marcela Carena, Stefania Gori, NausheenR. Shah, CarlosE.M. Wagner, and Lian-Tao Wang. Light stau phenomenology and the higgs $\gamma\gamma$ rate. *Journal of High Energy Physics*, 2012(7), 2012.

[27] Matthew R. Buckley, Joseph D. Lykken, Christopher Rogan, and Maria Spiropulu. Super-Razor and Searches for Sleptons and Charginos at the LHC. *Phys.Rev.*, D89(5):055020, 2014.

[28] John M. Campbell, R. Keith Ellis, and Ciaran Williams. Gluon-Gluon Contributions to W+ W- Production and Higgs Interference Effects. *JHEP*, 10:005, 2011.

[29] K.A. Olive and Particle Data Group. Review of particle physics. *Chinese Physics C*, 38(9):090001, 2014.

[30] A. Denner, S. Heinemeyer, I. Puljak, D. Rebuzzi, and M. Spira. Standard Model Higgs-Boson Branching Ratios with Uncertainties. *Eur.Phys.J.*, C71:1753, 2011.

[31] Robert Calkins and D Chakraborty. *Measurements of the Top Quark Pair Production Cross Section and Branching Ratio to a W-boson and bottom quark Using the Semi-Leptonic and Dilepton Final States with the ATLAS Detector at the LHC*. PhD thesis, Northern Illinois U., Oct 2012. Presented 18 Oct 2012.

[32] CERN. About cern. `http://home.web.cern.ch/about`, January 2015.

[33] CERN. The large hadron collider. `http://home.web.cern.ch/topics/large-hadron-collider`, January 2015.

[34] The CMS Collaboration. The CMS experiment at the CERN LHC. *Journal of Instrumentation*, 3(08):S08004, 2008.

[35] The ALICE Collaboration. The ALICE experiment at the CERN LHC. *Journal of Instrumentation*, 3(08):S08002, 2008.

[36] The LHCb Collaboration. The LHCb Detector at the LHC. *Journal of Instrumentation*, 3(08):S08005, 2008.

[37] AC Team. Diagram of an LHC dipole magnet. Schéma d'un aimant dipôle du LHC. Available at `"https://cds.cern.ch/record/40524`, Jun 1999.

[38] AC Team. The four main LHC experiments. Available at `"https://cds.cern.ch/record/40525`, Jun 1999.

[39] Measurement of the W^+W^- production cross section in proton-proton collisions at $\sqrt{s} = 8$ TeV with the ATLAS detector. Technical Report ATLAS-CONF-2014-033, CERN, Geneva, Jul 2014.

[40] Joao Pequenao. Computer generated image of the whole ATLAS detector. Mar 2008.

[41] W Lampl, S Laplace, D Lelas, P Loch, H Ma, S Menke, S Rajagopalan, D Rousseau, S Snyder, and G Unal. Calorimeter Clustering Algorithms: Description and Performance. Technical Report ATL-LARG-PUB-2008-002. ATL-COM-LARG-2008-003, CERN, Geneva, Apr 2008.

[42] Matteo Cacciari, Gavin P. Salam, and Gregory Soyez. The Anti-k(t) jet clustering algorithm. *Journal of High Energy Physics*, 0804:063, 2008.

[43] Joao Pequenao and Paul Schaffner. An computer generated image representing how ATLAS detects particles. Jan 2013.

[44] Collaboration ATLAS. Letter of Intent for the Phase-II Upgrade of the ATLAS Experiment. Technical Report CERN-LHCC-2012-022. LHCC-I-023, CERN, Geneva, Dec 2012. Draft version for comments.

[45] B T Huffman. Plans for the Phase II upgrade to the ATLAS detector. *Journal of Instrumentation*, 9(02):C02033, 2014.

[46] Letter of Intent for the Phase-I Upgrade of the ATLAS Experiment. Technical Report CERN-LHCC-2011-012. LHCC-I-020, CERN, Geneva, Nov 2011.

[47] L.A. Harland-Lang, C.H. Kom, K. Sakurai, and W.J. Stirling. Measuring the masses of a pair of semi-invisibly decaying particles in central exclusive production with forward proton tagging. *The European Physical Journal C*, 72(4), 2012.

[48] Daniel R. Tovey. On measuring the masses of pair-produced semi-invisibly decaying particles at hadron colliders. *Journal of High Energy Physics*, 2008(04):034, 2008.

[49] C.G. Lester and D.J. Summers. Measuring masses of semiinvisibly decaying particles pair produced at hadron colliders. *Phys.Lett.*, B463:99–103, 1999.

[50] Alan Barr, Christopher Lester, and P. Stephens. m(T2): The Truth behind the glamour. *J.Phys.*, G29:2343–2363, 2003.

[51] M. Serna. A short comparison between m_{T2} and m_{CT}. *Journal of High Energy Physics*, 6:4, June 2008.

[52] Serguei Chatrchyan et al. Inclusive search for supersymmetry using the razor variables in pp collisions at $\sqrt{s} = 7$ TeV. *Phys.Rev.Lett.*, 111(8):081802, 2013.

[53] Christopher Rogan. Kinematical variables towards new dynamics at the LHC. 2010.

[54] Simone Alioli, Paolo Nason, Carlo Oleari, and Emanuele Re. NLO Higgs boson production via gluon fusion matched with shower in POWHEG. *Journal of High Energy Physics*, 0904:002, 2009.

[55] Paolo Nason and Carlo Oleari. NLO Higgs boson production via vector-boson fusion matched with shower in POWHEG. *Journal of High Energy Physics*, 1002:037, 2010.

[56] G. Corcella, I.G. Knowles, G. Marchesini, S. Moretti, K. Odagiri, et al. HERWIG 6.5 release note. 2002.

[57] Stefano Frixione and Bryan R. Webber. Matching NLO QCD computations and parton shower simulations. *Journal of High Energy Physics*, 0206:029, 2002.

[58] Michelangelo L. Mangano, Mauro Moretti, Fulvio Piccinini, Roberto Pittau, and Antonio D. Polosa. ALPGEN, a generator for hard multiparton processes in hadronic collisions. *Journal of High Energy Physics*, 0307:001, 2003.

[59] R. Brun and F. Rademakers. ROOT: An object oriented data analysis framework. *Nucl.Instrum.Meth.*, A389:81–86, 1997.

[60] Performance assumptions based on full simulation for an upgraded ATLAS detector at a High-Luminosity LHC. Technical Report ATL-PHYS-PUB-2013-009, CERN, Geneva, Sep 2013.

[61] LHC Higgs Cross Section Working Group, S. Dittmaier, C. Mariotti, G. Passarino, and R. Tanaka (Eds.). Handbook of LHC Higgs Cross Sections: 1. Inclusive Observables. *CERN-2011-002*, CERN, Geneva, 2011.

[62] Rei Tanaka. Higgs cross sections for european strategy studies in 2012. `https://twiki.cern.ch/twiki/bin/view/LHCPhysics/HiggsEuropeanStrategy2012`, 2014.

[63] J Butterworth, E Dobson, U Klein, B Mellado Garcia, T Nunnemann, J Qian, D Rebuzzi, and R Tanaka. Single Boson and Diboson Production Cross Sections in pp Collisions at sqrts=7 TeV. Technical Report ATL-COM-PHYS-2010-695, CERN, Geneva, Aug 2010.

[64] W. Beenakker, M. Klasen, M. Kramer, T. Plehn, M. Spira, and P. M. Zerwas. The Production of charginos / neutralinos and sleptons at hadron colliders. *Phys. Rev. Lett.*, 83:3780–3783, 1999. [Erratum: Phys. Rev. Lett.100,029901(2008)].